Daily to centennial behavior of aseismic slip along the central section of the North Anatolian Fault

Romain Jolivet[1,1], Jorge Jara[2,2], Manon Dalaison[3,3], Bertrand Rouet-Leduc[4,4], Alpay Özdemir[5,5], Ugur Dogan[6,6], Ziyadin Çakir[7,7], Semih Ergintav[8,8], and Pierpaolo Dubernet[1]

[1]Ecole Normale Superieure
[2]Laboratoire de Geologie, ENS
[3]Ecole Normale Supérieure
[4]Los Alamos National Laboratory
[5]Yıldız Technical University
[6]Yildiz Teknik Universty
[7]Istanbul Technical University
[8]Bogazici University Kandilli Observatory and Earthquake Research Inst.

May 4, 2023

Abstract

Slow, aseismic slip plays a crucial role in the initiation, propagation and arrest of large earthquakes along active faults. In addition, aseismic slip controls the budget of elastic strain in the crust, hence the amount of energy available for upcoming earthquakes. The conditions for slow slip include specific material properties of the fault zone, pore fluid pressure and geometrical complexities of the fault plane. Fine scale descriptions of aseismic slip at the surface and at depth are key to determine the factors controlling the occurrence of slow, aseismic versus rapid, seismic fault slip. We focus on the spatial and temporal distribution of aseismic slip along the North Anatolian Fault, the plate boundary accommodating the 2 cm/yr of relative motion between Anatolia and Eurasia. Along the eastern termination of the rupture trace of the 1944 M7.3 Bolu-Gerede earthquake lies a segment that slips aseismically since at least the 1950's. We use Sentinel 1 time series of displacement and GNSS data to provide a spatio-temporal description of the kinematics of fault slip. We show that aseismic slip observed at the surface is coincident with a shallow locking depth and that slow slip events with a return period of 2.5 years are restricted to a specific section of the fault. In the light of historical measurements, we discuss potential rheological implications of our results and propose a simple alternative model to explain the local occurrence of shallow aseismic slip at this location.

Daily to centennial behavior of aseismic slip along the central section of the North Anatolian Fault

R. Jolivet[1,2], J. Jara[1], M. Dalaison[1], B. Rouet-Leduc[3], A. Özdemir[4], U. Dogan[4], Z. Çakir[5], S. Ergintav[6] & P. Dubernet[1]

[1]Laboratoire de Géologie, Département de Géosciences, École Normale Supérieure, PSL Université, CNRS UMR 8538, Paris, France
[2]Institut Universitaire de France, 1 rue Descartes, 75006 Paris
[3]Disaster Prevention Research Institute, Kyoto University, Kyoto, Japan
[4] Department of Geomatic Engineering, Yildiz Technical University, 34220 Istanbul, Turkey
[5]Department of Geology, Istanbul Technical University, 34469 Istanbul, Turkey
[6]Department of Geodesy, Kandilli Observatory and Earthquake Research Institute, Bogazici University, 34684 Istanbul, Turkey

Key Points:

- We image the spatio-temporal variations of aseismic slip along the central section of the North Anatolian Fault with InSAR and GNSS data
- Slow slip extends over 70 km, reaches 1 cm/yr and coincides with shallow locking depth along the fault
- Slow slip events do not occur along the whole creeping section but have been detected since, at least, the 1980's

Corresponding author: Romain Jolivet, `romain.jolivet@ens.fr`

Abstract

Slow, aseismic slip plays a crucial role in the initiation, propagation and arrest of large earthquakes along active faults. In addition, aseismic slip controls the budget of elastic strain in the crust, hence the amount of energy available for upcoming earthquakes. The conditions for slow slip include specific material properties of the fault zone, pore fluid pressure and geometrical complexities of the fault plane. Fine scale descriptions of aseismic slip at the surface and at depth are key to determine the factors controlling the occurrence of slow, aseismic versus rapid, seismic fault slip. We focus on the spatial and temporal distribution of aseismic slip along the North Anatolian Fault, the plate boundary accommodating the 2 cm/yr of relative motion between Anatolia and Eurasia. Along the eastern termination of the rupture trace of the 1944 M7.3 Bolu-Gerede earthquake lies a segment that slips aseismically since at least the 1950's. We use Sentinel 1 time series of displacement and GNSS data to provide a spatio-temporal description of the kinematics of fault slip. We show that aseismic slip observed at the surface is coincident with a shallow locking depth and that slow slip events with a return period of 2.5 years are restricted to a specific section of the fault. In the light of historical measurements, we discuss potential rheological implications of our results and propose a simple alternative model to explain the local occurrence of shallow aseismic slip at this location.

Plain Language Summary

Earthquakes are the manifestation of the rapid release of elastic energy stored in the crust under the action of moving tectonic plates on either sides of a fault system. Interestingly, some faults release energy under the form of aseismic slip, which is slow and harmless. The conditions for slow slip, as opposed to earthquakes, are not fully understood and it appears of higher importance to study high-resolution, small scale features to grow our understanding. We analyze satellite Radar imagery and GNSS data to build a movie of ground motion in the vicinity of the North Anatolian Fault in Turkey over a section that was recognized to slip aseismically in the 70's. We show that aseismic slip there is made of slow slip events repeating every 2.5 years embedded within a larger region that slips steadily. Using these data, we model the distribution of slip rates at depth on the fault and show that aseismic slip extends until 5-8 km depth. Below, the fault is locked, accumulating energy for upcoming earthquakes. In the light of past measurements and based on our high-resolution dataset, we discuss potential physical models explaining the occurrence of slow slip in this region.

1 Introduction

The discovery of slow, aseismic slip in the 1960's both along the San Andreas Fault (Steinbrugge et al., 1960) and the North Anatolian Fault (Ambraseys, 1970) led to a revision of the elastic rebound theory proposed by Reid (1911). Slow slip has now been described along numerous active faults, including the San Andreas Fault (e.g. Steinbrugge et al., 1960; Jolivet, Simons, et al., 2015), the North Anatolian Fault (e.g. Ambraseys, 1970; Çakir et al., 2005), the Leyte fault (e.g. Duquesnoy et al., 1994; Dianala et al., 2020) among others (see a complete description in Jolivet and Frank (2020)), and is now recognized as one end-member mode of fault slip releasing stress along active faults. Slow slip has also been described along subduction megathrust either in the form of transient events (e.g. Dragert et al., 2001; Wallace, 2020), associated with tremors or not, and as variations of megathrust kinematic coupling (e.g. Mazzotti et al., 2000; Avouac, 2015). Observationally, slow slip has been linked with the preparation phase of earthquakes, such as before the M_w8.1 Iquique earthquake in Chile in 2014 (e.g. Ruiz et al., 2014; Socquet et al., 2017) or, more disputably, before the M_w7.4 Izmit earthquake in 1999 in Turkey (Bouchon et al., 2011; Ellsworth & Bulut, 2018). Effectively, slow slip, like earthquakes, contributes to the release of elastic energy that accumulates under the loading imposed by tectonic motion (e.g. Avouac, 2015). As a result, slow slip influences the size of large earthquakes which are known to be arrested preferentially by fault segments hosting aseismic slip (e.g. Kaneko et al., 2010), among other causes.

Although the importance of aseismic slip on the dynamics of earthquakes is indisputable (e.g. Avouac, 2015; Bürgmann, 2018), the physical mechanisms responsible for keeping slip slow are still unclear. Multiple mechanisms may be involved to prevent fault slip to become dynamic and reach slip speeds characteristic of earthquakes ($\sim$ 1 m/s). First, the spatial distribution of rheological properties of the fault material governs the spatial and temporal evolution of fault slip. For instance, rate strengthening fault material leads to stable slip (e.g. Scholz, 1998; Thomas et al., 2017). As fault rheology, and in particular the constitutive properties of the law controlling friction on the fault plane, depends on temperature and normal stress, the resulting depth-dependent distribution of fault properties explains the depth distribution of slip modes in a variety of subduction zones and continental faults (e.g. Blanpied et al., 1991; den Hartog & Spiers, 2013). Second, if fault frictional properties lead to a rate weakening behavior, a large nucleation size (i.e. the slip distance over which slip becomes dynamic) may prevent slip to reach seismic speeds (e.g. Ampuero & Rubin, 2008). As nucleation size depends on both constitutive properties and effective normal stress, one may invoke the influence of elevated pore fluid pressure to keep slip stable, as observed at the deep end of the potentially seismogenic portion of subduction megathrust (e.g. Kodaira et al., 2004; Moreno et al., 2014). Third, recent works suggest that complexities in the fault geometry may lead to the emergence of slow slip even with unstable rate-weakening properties, either through local modulation of normal stress due to slip on a rough fault (Cattania & Segall, 2021) or to stress interactions between fault segments (Romanet et al., 2018). In all cases, it is important to realize that the geological conditions underlying these physical mechanisms may vary over a wide range of length scales. Rock types, pore fluid pressure and fault geometry may vary over any distances, from millimeters to hundreds of kilometers. Fault geometry for instance is considered self-similar and has no characteristic length scale (e.g. Candela et al., 2012).

It is therefore of uttermost importance to provide descriptions of aseismic, slow slip with the highest level of details over large regions. In subduction zones, the vast majority of geodetic and seismological stations are necessarily located on land, far from the megathrust. To the contrary, the surface expression of continental faults can be studied with high levels of detail due to available Interferometric Synthetic Aperture Radar (InSAR) data, near-field GNSS stations and creepmeters, which may reveal the smallest details of aseismic slip. For instance, Jolivet, Candela, et al. (2015) and Khoshmanesh and Shirzaei (2018) have explored the occurrence of clusters of slow slip events with scales from tens of meters to tens of kilometers, suggesting an avalanche-like behavior witnessing interactions between slow slip events. As another example, Dalaison et al. (2021) show the complex pattern of slow and rapid slip along the Chaman fault in Pakistan which hosts one of the longest creeping sections on Earth. In this paper, we explore and describe the behavior of aseismic slip along the Ismetpasa section of the North Anatolian Fault (Fig. 1), covering time scales ranging from days to decades and length scales from hundreds of meters to tens of kilometers.

2 Seismo-tectonic setting and motivation

First mentions of aseismic slip along the North Anatolian Fault date from Ambraseys (1970). In particular, Ambraseys (1970) describes the offset of a wall in the city of Ismetpasa which was not related to any significant seismic activity. Although the paper mentions that it is not known whether the offset occurred gradually or episodically, a mean creep rate of 2 cm/yr was inferred while the earlier offset of railroad tracks in the vicinity suggested a 5 cm/yr creep rate from 1944 to 1950. Following the suggestion of Ambraseys (1970), Bilham et al. (2016) re-evaluated these surface slip rates, inferring slightly slower rates. The 1944 M 7.4 Gerede earthquake is the last large event known to have ruptured in this area, and those early estimates fall within the subsequent post-seimic period (e.g. Fig. 1 and Kondo et al., 2010). Since then, numerous studies have measured surface slip rates, using land-based and geodetic techniques, including creep-meters, GNSS data and InSAR data (Aytun, 1982; Eren, 1984; Deniz et al., 1993; Altay & Sav, 1991; Çakir et al., 2005; Kutoglu & Akcin, 2006; Kutoglu et al., 2008, 2010; Karabacak et al., 2011; Deguchi, 2011; Kaneko et al., 2012; Ozener et al., 2013; Cetin et al., 2014; Bilham et al., 2016). All subsequent studies infer a surface creep rate, at Ismetpasa, of about 6 to 8 mm/yr, since at least the 1980's. The decrease in slip rate from 5 cm/yr followed by a rather constant rate of 6 to 8 mm/yr was interpreted as the signature of a long lived post-seismic signal and modeled with rate-and-state friction (Kaneko et al., 2012). The model suggests that shallow material, from the surface to a depth of about 5 km, is rate-strengthening, promoting shallow afterslip. Prompting adequate tuning of the constitutive parameters of the friction law, this model can produce long lived afterslip lasting more than 55 years. It is important to realize that all these measurements were made and restricted to a single location along the fault and that the slip rates measured directly following the 1944 earthquake are uncertain (Bilham et al., 2016).

Slow slip events were recently discovered at Ismetpasa (Bilham et al., 2016; Rousset et al., 2016). In 2013, a 2 cm slow slip event was detected from time series analysis of InSAR data acquired by the Cosmo-Skymed constellation (Rousset et al., 2016). Slip spanned a 10 km-long section of the fault with a 4 km width along dip. Such event echoes the surface slip accelerations inferred from creepmeter records in the 1980's (Altay & Sav, 1991) and those currently captured by the creepmeter operating since 2014 (Bilham et al., 2016). The largest slow slip events are spontaneous as they do not follow significant earthquakes or identified stress perturbation. They repeat every 2 to 3 years with slip amplitudes that vary from 5 to 15 mm. These events were not accounted for as such in early measurements of surface slip rates (e.g. Altay & Sav, 1991) and are most likely averaged into such rates. In addition, we do not know the full spatial extent of these slow slip events. Finally, the presence of such events suggests that the rheology of the fault at shallow depth cannot be uniformly rate-strenghtening and two possibilities arise. Rheology is either rate-weakening, hence promoting spontaneous slip instabilities although such instabilities must remain slow, or rheology is heterogeneous with unstable fault patches embedded in a generally stable matrix (Wei et al., 2013).

In all cases, several questions are left unanswered considering the slip rate variations and distribution along the creeping section of Ismetpasa. First, although the spatial distribution of slip has already been inferred (Cetin et al., 2014), it is unclear how deep slip extends and what are the uncertainties associated with the slip distribution. Large scale strain mapping and modeling are not sufficient and fine exploration of the deformation field in this area is required (Weiss et al., 2020; Barbot & Weiss, 2021). Second, temporal variations of slip rate have, so far, only been detected at Ismetpasa. Is such episodic behavior representative of the whole fault section or not?

To address these questions, we derive time series of surface displacements over the 2014-2021 period from Sentinel 1 InSAR data and explore the spatial and temporal behavior of aseismic slip along this creeping section. We also include ground velocity measured at GNSS sites from the National Turkish network and preliminary results from a network of near-fault GNSS sites designed to capture slow slip events. In the following, after specifying our approach, we describe the resulting surface velocity field and infer the distribution of average slip rates at depth along with associated uncertainties. We then explore potential surface slip rate variations to detect small slow slip events over the whole extent of the creeping section. We finally discuss the occurrences of such slow events in the light of previously measured surface slip rates and elaborate on the rheology of the fault zone.

3 Data processing

3.1 InSAR data processing

We process all available Synthetic Aperture Radar data from the Sentinel 1 constellation from 2014 to late 2020 with the ISCE processing environment (JPL/Caltech, `winsar.unavco.org/isce.html`; Gurrola et al., 2010) using the same approach as Dalaison et al. (2021). We process data from descending tracks 65 and 167 and ascending track 87. First, we coregister all images to a single reference acquisition chosen in the middle of the time series of images. Coregistration is performed using satellite orbits and refined using the spectral diversity available on Radar burst overlaps (Fattahi et al., 2016). From the 288, 278 and 293 acquisitions on tracks 65, 167 and 87 respectively, we then compute 1858, 1826 and 3053 interferograms (see supplementary figures S-1 to S-3 for baseline plots). We remove the contribution of the stratified tropospheric delay from the wrapped interferograms using the ERA5 re-analysed temperature, water vapor and pressure level heights fields (Jolivet et al., 2011, 2014) using the PyAPS software (Agram et al., 2013). We look down interferograms for a final pixel size of about 120 m in azimuth and range direction (i.e. 8 looks in azimuth and 32 looks in range). We then filter and unwrap interferograms using the adaptive phase filter and the coherence-based branch cut algorithm available in ISCE (Goldstein et al., 1988; Goldstein & Werner, 1998). We finally correct for potential unwrapping errors using the CorPhu algorithm (Benoit et al., 2020). Independently on each track, we use the Kalman filter approach developed by Dalaison and Jolivet (2020) to reconstruct the time series of surface displacements in the satellite Line-Of-Sight (hereafter LOS) from the set of interferograms. Since no significant earthquake has been detected in the region over the period we analyse, we only consider an annual oscillation and a secular trend as a basis model underlying the Kalman filter. We use the parameterization proposed in Dalaison and Jolivet (2020).

Results are shown on Fig. 1 and S-4 to S-15 of the supplementary informations. As interferograms do not unwrap completely, with especially poor coherence in the north of the area close to the shore of the Black Sea, final reconstruction of the time series shows variable quality. We define the reconstruction Root Mean Square (RMS) as the square root of the sum of the squared difference between the interferograms and the synthetic interferograms inferred from our time series, divided by the total number of interferograms. We compute such RMS for each pixel of each track (Figures S-13 to S-15 of the supplementary informations). We decide to mask pixels with a reconstruction RMS higher than 2 mm, pixels constrained by less than 1300 interferograms (Figures S-10 to S-12 of the supplementary informations) and with a final uncertainty on the velocity higher than 0.5 mm/yr (Figures S-7 to S-9 of the supplementary informations). We retain for the following analysis pixels less than 60 km away from the North Anatolian Fault trace. We combine the final three LOS velocity maps into fault parallel and vertical velocity maps assuming horizontal motion aligns with 77.5°N azimuth (Dalaison et al., 2023). Final horizontal velocity is shown on Fig. 1 while the vertical velocity map is available on Fig. S-18 of the supplementary materials.

Similar to Dalaison et al. (2021), we extract fault perpendicular profiles on each LOS velocity maps every 250 m and evaluate the across fault ground velocity difference to infer the surface slip rate and the associated uncertainties (Fig. S-16 and Fig. S-17 of the supplementary materials). Such slip rate is remarkably consistent between both descending tracks 65 and 167 and shows opposite sign on track 87, suggesting a dominantly strike slip motion across the fault. We combine these along strike surface slip measurements into a strike slip and dip slip motion (Fig. 1 and Fig. S-17 of the supplementary materials). Potential dip slip is visible between 32.5°and 32.75°W of longitude, near Ismetpasa.

3.2 GNSS data processing

We installed 19 permanent GNSS sites along the section previously identified as creeping by Cetin et al. (2014). Sites are located close to the fault ($<$ 5 km) in order to capture shallow slow slip events, previously captured with InSAR and creepmeter data (Altay & Sav, 1991; Bilham et al., 2016; Rousset et al., 2016). In this paper, we only seek to include velocities measured at each site of this network, hereafter referred to as Ismenet, to constrain the slip rate at shallow depths. A detailed description of the typical site setup we implemented with station measurement periods can be found in the supplementary informations. We processed data from the Ismenet network together with 57 stations from the International GNSS service (37 sites, `www.igs.org`) and from the Turkish National Network (20 sites, `https://www.tusaga-aktif.gov.tr/`). A detailed description of the sites used can be found in supplementary materials.

Observations are processed in double differences using the GAMIT/GLOBK 10.7 software (Herring et al., 2018) to obtain daily estimates of station positions, choosing ionosphere-free combination and fixing the ambiguities to integer values. We use precise orbits from the International GNSS Service for Geodynamics, precise EOPs from the IERS bulletin B, IGS tables to describe the phase centers of the antennas, FES2004 ocean-tidal loading corrections, and atmospheric loading corrections (tidal and non-tidal). One tropospheric vertical delay parameter and two horizontal gradients per stations are estimated every 2 hours. We use the GLOBK software (Herring et al., 2015) to combine daily solutions and the PYACS software (Nocquet, 2018a) to derive the position time series, which are then mapped into the ITRF 2014 reference frame (Altamimi et al., 2016). Finally, the time series are set in a fixed Eurasian frame, considering the pole solution proposed by Altamimi et al. (2016). We use a trajectory model to extract the velocity on each time series (Bevis & Brown, 2014) and evaluate the standard deviation on velocities assuming white and flicker noise following Williams (2003).

4 Surface velocity and average slip rate

4.1 Surface velocity across the North Anatolian Fault

Our velocity map is consistent with previously published results (e.g. Kaneko et al., 2012; Cetin et al., 2014). Although decoherence and poor RMS reconstruction leaves gaps in the velocity map, we clearly identify the signature of the North Anatolian Fault with a gradient of ~ 2 cm/yr across the fault which varies significantly along strike (Fig. 1, 2 and S-16). Along most portions of the fault, the across fault gradient of displacement rate is gradual with a 20-30 km-wide transition from westward to eastward motion (i.e. west of 32.4°E and east of 33.4°E).

Between 32.4°E and 33.4°E, we observe a very sharp, step-like gradient of velocity across the fault both in the InSAR-derived fault parallel velocity map and in the GNSS-derived velocities (Fig. 1 and 2). We interpret this step-like transition as the signature of surface slip over an approximately 60 to 70 km-long profile. This surface slip rate shows a maximum slip rate of 1 ± 0.2 cm/yr that tappers down laterally to negligible values in an almost elliptical shape. Slip rate at the city of Ismetpasa (longitude 32.63°E) is 6 ± 2 mm/yr, consistent with published rates from creepmeter measurements (Bilham et al., 2016). Uncertainties are on the order of 2 to 3 mm/yr. The distribution of slip at the surface overlaps with both the eastern termination of the 1944 Bolu-Gerede (M_w7.4) earthquake and the western end of the 1943 Tosya (M_w7.6) earthquake (Kondo et al., 2005; Barka, 1996). This segment also overlaps with the rupture of the 1951 Kursunlu M_w6.9 earthquake, although the extent of that rupture is unclear (Ambraseys, 1970; Barka, 1996).

We observe significant vertical differential motion across the fault near the city of Ismetpasa, where the northern block subsides with respect to the southern block (Fig. 1). The rate of vertical differential motion reaches locally 12 ± 3 mm/yr but its extent does not exceed 15 km along strike. We also observe pronounced subsidence north of the fault, with a maximum of 10 mm/yr, over a 15 km-wide region bounded by the trace of the North Anatolian Fault to the south (Fig. 1). We account for this subsidence signal in further modeling in order not to bias slip rate estimates at depth. This subsidence signal overlaps with cultivated land, suggesting potential hydrological effects related to water pumping. Other signals of vertical motion can be observed in various places in the velocity map but further away from the fault (> 20 km), hence these should average out in the data decimation process and not affect our model inference. We do not observe any other subsidence signal along the fault trace. Finally, we raise the readers' attention to the fact that such subsidence is observed where previous local measurements of aseismic slip were done.

4.2 Slip distribution and uncertainties

The surface velocity field described above is consistent with strain localizing in the vicinity of a major strike slip, plate boundary fault. We do not observe significant signals associated with other faults, hence we assume surface displacement rates originate from slip along the North Anatolian Fault at depth. Following the approach of Jolivet, Simons, et al. (2015), we consider the NAF as a vertical fault embedded in an elastic crust. Surface displacement resulting from elastic loading is usually modeled as the result of slip on an infinitely deep dislocation buried below a given locking depth (Savage & Burford, 1973). Aseismic slip can be modeled as the result of shallow elastic dislocations (e.g Ryder & Bürgmann, 2008; Maurer & Johnson, 2014; Jolivet, Simons, et al., 2015; Bletery et al., 2020). Finally, local subsidence can be modeled using an *ad hoc* Mogi source with a pressure or volume change (Mogi, 1958).

We model the surface displacement captured by the three InSAR line-of-sight velocity maps and by our local GNSS network as the sum of 4 contributions. Note that, here, we do not use the horizontal and vertical motion maps but directly the LOS velocity maps. First, we solve for strike slip rate on infinitely deep dislocations following the trace of the NAF buried below 20-km-depth. This depth is chosen deep enough to reach the brittle-ductile transition and to allow shallower slip on the shallow portion of the NAF in case the effective locking depth is located above 20-km-depth. Second, we discretize the NAF fault plane above the locking depth up to the surface in a triangular mesh. Slip on this fault plane is the linear interpolation of slip values at each node of the triangular mesh. Triangle sizes vary from 1 km at the surface to 10 km at depth (see supplementary informations Fig. S-29). Third, we model local vertical motion across the NAF at Ismetpasa by dip slip motion on a subset of the mesh used for strike slip. For all fault models, we compute Green's functions relating slip to surface displacements in a semi-infinite stratified half-space using the stratification of elastic parameters from Rousset et al. (2016). Fourth, we include a Mogi source at an arbitrary depth of 3 km below the subsiding basin north of Ismetpasa (Mogi, 1958). We include this source to remove the potential bias on the inferred strike slip rate. We are not interested in the actual values of pressure change in the source which tradeoff with its depth and size, hence the arbitrary choice of the depth of the source.

In addition, we model long wavelength signals in each InSAR velocity maps (i.e. orbital errors, long wavelength atmospheric signals, etc) as a linear function of longitude and latitude. We also solve for a translation and a rotation within the GNSS velocity field. These geometrical transformations allow to place the data in a reference frame in which displacement rates are null on top of the fault, consistently with our setup. Final parameter set includes slip rate on deep dislocations to model crustal elastic loading, slip rate on the shallow, discretized NAF, dip slip in the vicinity of Ismetpasa, a Mogi source north of Ismetpasa and geometric parameters for InSAR and GNSS common referencing.

We downsample the InSAR velocity maps to minimize computational burden using a quadtree approach designed to maximize resolution on the fault plane (Lohman & Simons, 2005; Jolivet, Simons, et al., 2015). In order to avoid averaging velocities across the fault, we exclude pixels located less than 1 km from the fault trace. Doing so, we lose precious information on potential slip along the shallowest portion of the fault ($<$ 1 km-depth). We therefore model the across fault step measured in the three LOS velocity maps and we force slip to be constant between the surface and a depth of 1 km. Moreover, to ensure continuity of slip rates at depth, we constrain slip rates along the deepest elements of the meshed NAF to equal those along the deep dislocations.

We explore the range of possible models using a Bayesian approach in order to derive the posterior Probability Density Function of models. Effectively, the posterior PDF, $\Theta(\mathbf{m}|\mathbf{d})$, is proportional to the product of the prior PDF (i.e. our state of knowledge before considering any data), $\rho(\mathbf{m})$, with the likelihood (i.e. the probability that a model will lead to a prediction that fits the data), $L(\mathbf{d}|\mathbf{m})$, according to Bayes' theorem, such as

$$\Theta(\mathbf{m}|\mathbf{d}) \propto \rho(\mathbf{m})L(\mathbf{d}|\mathbf{m}), \tag{1}$$

where $\mathbf{m}$ is the vector of model parameters and $\mathbf{d}$ is the data vector. As a prior PDF, we consider a uniform distribution from 0 to 50 mm/yr for strike slip on the shallow part of the NAF. Since most plate reconstruction models suggest a long term slip rate of the NAF around 20 mm/yr (e.g. DeMets et al., 2010), we consider a uniform distribution between 10 and 30 mm/yr for the deep dislocations. We consider uniform distributions for the parameters of the geometric transformations applied to each of the geodetic datasets. We chose a Gaussian formulation for the likelihood such as

$$L(\mathbf{d}|\mathbf{m}) \propto \exp -\frac{1}{2}(\mathbf{Gm}-\mathbf{d})^T\mathbf{C}_\chi^{-1}(\mathbf{Gm}-\mathbf{d}), \quad (2)$$

where $\mathbf{G}$ is the matrix of Green's functions. Following the approach of Duputel et al. (2014), $\mathbf{C}_\chi$ is the sum of $\mathbf{C}_d$, the data covariance matrix, and $\mathbf{C}_p$, the matrix of prediction uncertainties accounting for uncertainties in the elastic structure (see Rousset et al., 2016, for a description of how we build $\mathbf{C}_p$). We build the data covariance matrix assuming different datasets (i.e. InSAR and GNSS velocities) are independent. We evaluate the covariance of the InSAR velocity maps over regions with no identified deformation signals (e.g. Sudhaus & Jónsson, 2009; Jolivet, Simons, et al., 2015, and supp. mat. Fig. S-30). Effectively, since we retain InSAR data less than 60 km away from the fault, we expect InSAR data to constrain mostly the distribution of shallow slip while far field GNSS velocities should constrain the deep slip rate.

Since we use bounded uniform and Gaussian prior PDFs, there is no analytical formulation of the model that best fits the data, although a bounded normal distribution is expected (Nocquet, 2018b). We use AlTar, a stochastic sampler using elements of parallel tempering, to draw 90,000 samples from the posterior PDF (`https://github.com/AlTarFramework/altar`; Minson et al., 2013; Jolivet, Simons, et al., 2015). Doing so, we explore the range of models that explain the data without the use of any form of regularization (i.e. smoothing) apart from the choice of the geometry of the fault (i.e. as opposed to trans-dimensional methods, Dettmer et al., 2014). AlTar uses parallel tempering to let the sample set slowly converge toward the posterior PDF. Here, we need 62 iterations to let the 90,000 Markov chains converge (see Fig. S-28 for an example of convergence for the marginal of the deep slip rate on the NAF).

In figure 3, we show the mean of the 90,000 samples and the corresponding standard deviation. First, we see that the slip rate on deep dislocations is 20±0.6 mm/yr, consistent with the expected relative pate motion rate at this location. Second, we observe that, given the large size (> 5 km) of triangles of the fault mesh at the bottom end of the shallow section of the NAF, locking depth can be effectively anywhere between 15 and 20 km everywhere along the fault, except where surface aseismic slip is observed. Third, below the 60-70 km long segment that slips rapidly at the surface between Ismetpasa and Bayramoren, we observe a shallower locking depth between 8 and 12 km. Along this segment, slip rates locally reach 20±3 mm/yr with potentially two distinct slip patches. In addition, along this same section, we observe a locked section at depth from roughly 5 to 10 km-depth. Near the city of Ismetpasa, we observe a patch of dip slip with slip rates as high as 12±3 mm/yr, although this patch is very limited in size. Other along strike variations of slip rate are not significant compared to the standard deviation and correspond to areas where InSAR decoherence led to poor surface velocity reconstruction. Figures S-24, S-26 and S-31 to S-34 of the supplementary informations show how the mean model performs at fitting the data. Note that the mean model does not belong to the ensemble of models drawn from the posterior PDF and is expected to show lower performance than models actually within our sample set. Since the posterior PDF is expected to be a multivariate bounded Gaussian distribution, the mean model should not be too different from the best fit model.

As a conclusion, the distribution of slip rates along the NAF in the region of Ismetpasa can be summarized as (1) a rapidly slipping segment east of Ismetpasa extending over 60-70 km with slip rates as high as 20 mm/yr, (2) a shallow locking depth between 8 and 12 km-depth below the segment of Ismetpasa and (3) a locking depth between 15 and 20 km-depth elsewhere (Fig. 3).

5 Time-dependent surface slip

We explore time-dependent surface slip as directly measured in the InSAR time series. We apply a similar approach to Dalaison et al. (2021) to extract shallow slip along the NAF from the time series of LOS displacements. We first extract, 500 m-wide, fault perpendicular profiles of LOS displacements every 250 m along the NAF at each acquisition time of each of the three time series on tracks 65, 87 and 167. We then extract the across fault step in LOS displacement and interpolate these values in time and space to combine them into time series of strike slip (i.e. fault parallel slip component) and dip slip (i.e. across fault vertical differential motion).

We show in Figure 4 the space and time evolution of surface slip along the section where aseismic slip has been identified in previous studies. In addition, we apply the deep denoiser developed by Rouet-Leduc et al. (2021) in order to detect the most important variations of surface slip. This denoiser is a trained convolutional neural network specifically designed to remove tropospheric artefacts from time series of LOS apparent displacements. Effectively, the denoiser removes what is identified as noise (i.e. here Gaussian correlated noise, topography correlated phase values and isolated pixels showing anomalous values wrt. their surrounding pixels) and highlights surface displacement consistent with those produced by dislocations embedded in an elastic halfspace. Moreover, this procedure reveals signals that are consistently growing with time, unlike tropospheric artefacts. Here, we show the instantaneous slip rate as measured on the output of the denoiser, considering the time spanned by the acquisitions used as input to the neural network. Finally, these results are compared with ground-truth measurements from a local creepmeter (Bilham et al., 2016). In supplementary informations figures S-19 and S-21, we show the uncertainties associated with the strike slip estimates and the vertical differential motion across the fault.

The history of strike slip along the aseismic section extending east of Ismetpasa shows along strike variations. We observe slip rate accelerations and decelerations over a 30 km-long section of the NAF, extending from 10 km west (Lon 32.5°) to 20 km east (Lon 32.85°) of Ismetpasa. Surface slip events lasting a few days to a few weeks can be seen, for instance from +10 km to +20km from Ismetpasa early 2016 in Figure 4. Some of these slip events are also captured by the creepmeter in Ismetpasa, such as the ~ 5 mm slip events in mid-2017 and late 2020 (Fig. 4). These events are visible in the surface slip evolution in Figure 4 at Ismetpasa (km 0). The denoiser detect these two transients, which display similar along-strike length as the event detected in 2013 by Rousset et al. (2016) and cleaned up by Rouet-Leduc et al. (2021). Their spatial extent is directly visible in the time series (Fig. S-22 of supplementary materials) although it does not stand out clearly enough from the noise to allow us to model their depth extent. The corresponding denoised surface displacements is not helpful to constrain the depth extent as the neural network is yet unable to recover the long wavelength of a deformation field (Rouet-Leduc et al., 2021).

Interestingly, we do not observe transient slip accelerations over the easternmost section. From 20 to 75 km east of Ismetpasa, we record steady surface slip with no obvious slow slip events. The denoiser also does not capture sudden slip accelerations, suggesting that slow slip events are not hidden in the noise of our time series. If occurring, slow slip events may be too small to be recorded by InSAR. More sensitive, local instruments such as creep- or strain-meters should be installed.

Vertical differential motion across the fault observed in the westernmost section also does not show sudden accelerations (Fig. S-21). Potential periodic signals in the vertical differential motion can be seen in the central section between +20 km and +30 km, although the corresponding variations are small (i.e. less than 4 mm) hence should be taken with caution. No significant differential vertical motion is observed east of +40 km of the section.

6 Discussion

As a summary, the central section of the North Anatolian Fault can be characterized by the presence of a 60 km-long section that slips continuously since, at least the 1980's (Altay & Sav, 1991). Since no significant seismicity is observed along the section at least since the 60's, slip is considered to be mostly aseismic. Slow slip events are observed every 2.5 years with 5 to 15 mm of slip at the surface over the westernmost part of the aseismic segment. The eastern part of the segment slips continuously at rates reaching 1 cm/yr, half of the relative plate motion expected at this location. At depth, aseismic slip extends from the surface to a depth of 5 to 6 km. Below, the fault is locked over a 4 to 5 km-wide portion. The locking depth below this aseismic section is relatively shallow, 12 km, compared to the 15 to 20 km observed elsewhere along the fault where no surface aseismic slip is observed.

6.1 Consistency of creepmeter and InSAR measurements

The first notable element of discussion is the accuracy and precision of both InSAR data and creepmeter measurements. Creepmeters installed in Ismetpasa measure relative displacement over a 20 m (Altay & Sav, 1991) or 16.6 m (Bilham et al., 2016) distance with a 30°angle with respect to the local orientation of the NAF (Altay & Sav, 1991; Bilham et al., 2016). One could argue that these instruments would measure very local fault slip, spanning a very shallow depth along dip. Our InSAR data show that both slow slip averaged over several years of measurements and the slow slip events captured by the creepmeters actually extend for several kilometers along strike. The 2013 slow slip event, even though not captured by creepmeters as no instrument was installed at the time, is 5-8 km-long and extends down to 4 km at depth Rousset et al. (2016). Events captured by our time series of InSAR data are of comparable along-strike extent and slip. Furthermore, InSAR time series have 120 m-sized pixels and we evaluate surface slip by linear regression of the InSAR data over several kilometers on both sides of the fault. Therefore, the slow slip events captured by our InSAR time series are probably spanning the first kilometers at depth, although our data is too noisy to allow accurate slip modeling. This means that the largest events captured by creepmeters are indeed spanning several kilometers at depth, a depth much larger than the creepmeter baseline length would lead to consider. Such consistency between different measurement methods also leads to conclude that, to first order, there is no significant variations in slip at depth during the slow slip events at Ismetpasa between the surface and a depth of 1 to 2 km.

We note that slip events captured by the creepmeter prior to 2016 are neither visible in our InSAR time series, although a slight long term trend is visible, nor detected by our neural network (Fig. 4). These events could be local and affect a section of the fault too small to be detected by InSAR. During the 2014-2016 period, only one Sentinel 1 satellite (Sentinel 1-A) was operational and the frequency of SAR acquisitions only doubled with the launched of Sentinel 1-B. The lower sensitivity to mm-to-cm slip events during the 2014-2016 could also be related to such lower rate of repetition of acquisitions.

6.2 time-dependent slow slip and the rheology of the aseismic section

Comparing results with previously published ones, the along strike distribution of surface slip rates we infer is comparable to that measured by Cetin et al. (2014) and Kaneko et al. (2012) with Envisat data over the 2003-2010 period. We observe a gradual increase in slip rates east of Ismetpasa, reaching up to 1 cm/yr, and a decrease further east over the 60 km-long segment. The only notable exception is a 10 km-long fast slipping section observed by Cetin et al. (2014) in the 2003-2010 data with rates as high as 2 cm/yr, 20 to 30 km east of Ismetpasa. Such high rates have not been described by Kaneko et al. (2012) with the same data. In addition, we observe that, over the 2014-2020 period, slip rates to the east of Ismetpasa are remarkably stable with no significant temporal variations. As no ground-based measurements are available for that part of the fault, we have to compare InSAR measurements inferred from data acquired by different satellites and processed with different techniques. For instance, Cetin et al. (2014) used a persistent scatterer method to process the data and obtained fewer pixels compared to our SBAS-like approach but with a potentially higher precision in the velocity measurement. Although it would be tempting to conclude on a local drop in velocity from 2 to 1 cm/yr in the central part of the section between the periods covered by Envisat data (2001-2010) and by Sentinel 1 data (2014 onwards), we prefer to remain cautious on this point because of the inconsistency between measurements by Cetin et al. (2014) and Kaneko et al. (2012). The relative temporal stability of surface slip over the 2014-2020 period actually advocates for a stable slip rate over the last 2 decades.

Near Ismetpasa, early creepmeter measurements revealed the occurence of slow slip events in the 1980's (Altay & Sav, 1991). Comparable accelerations are described by Rousset et al. (2016) and Bilham et al. (2016) in 2013 and 2014-2016. As rightly pointed out by Bilham et al. (2016), aliasing of measurements with different and potentially uneven temporal sampling leads to different conclusions. That said, over periods of several days, rates vary by one to two orders of magnitude as shown in figure 5. Averaging over years of measurements, the slip rate at Ismetpasa is, to the contrary, remarkably stable, although a slight decay may be considered (Fig. 5). After a revisit of the measurement of the original wall offset by Ambraseys (1970), Bilham et al. (2016) proposed a corrected estimate of the surface slip rate in the 1960's of 1 cm/yr. In addition, Bilham et al. (2016) discards the early measurement of an offset in railroad tracks as deemed too uncertain, in agreement with the original report by Ambraseys (1970). Using the corrected slip rates from Bilham et al. (2016), one may consider a decrease in averaged slip rates (Fig. 4), from 1 cm/yr in 1970 to 6$\pm$2 mm/yr in 2020. A bayesian linear regression through the velocity estimates suggests a deceleration of 0.07$\pm$0.01 mm/yr^2 from 1960 to 2020. However, the uncertainty provided with the measurement on the wall photograph from 1969 is 0.4 mm/yr, a value probably too small for such measurement. Similar concern may be raised for other measurements with uncertainties lower than one mm/yr based on historical photographs. Considering uncertainties might have been underestimated, the decrease in slip rate at Ismetpasa is not statistically significant anymore.

Therefore, since the slip rate estimate inferred by Ambraseys (1970) for the 1944-1950 time period has been discarded by Bilham et al. (2016) as too uncertain, the hypothesis of a long standing post-seismic decay put forward by Kaneko et al. (2012) and Cetin et al. (2014) becomes difficult to accept. The expected logarithmic decay of slip rates following a large earthquake is not shown by the data as only a slight decrease in slip rates is visible from 1960 to today. We cannot discard the hypothesis that afterslip occurred after the 1944 earthquake, as would be expected for such a large earthquake, but we simply cannot reject nor support this hypothesis with the available data. Conditions for such post-seismic afterslip are the presence of a locked, seismogenic asperity at depth, as confirmed by our and previously published analysis (e.g. Cetin et al., 2014; Bilham et al., 2016), and the presence of rate-strengthening material near the surface. The depth-dependence of constitutive parameters of friction laws suggests that rate-strengthening material is to be expected near the surface (e.g. Blanpied et al., 1991; Scholz, 1998), but is not confirmed by geodetic data here as no obvious post-seismic signal is observed.

If constitutive properties of the fault were to explain the occurrence of aseismic slip along this section, then it would also require along strike rheological variations in addition to the expected depth-dependency. Rocks exposed at the surface along the aseismic segment include volcanic deposits, sedimentary units (limestones) and metamorphic rocks (Cetin et al., 2014), suggesting no specific link between rock type and slip behavior. Kaduri et al. (2019) propose a relationship between the development of a specific mineralogical fabric in the fault material and the occurrence of aseismic slip, suggesting that the peculiar slip behavior of this segment, compared to the rest of the NAF that ruptured during the 1944 and 1943 earthquakes, may be related to the occurrence of pressure solution creep in the fault gouge. Similar observations have been made along the Longitudinal Valley fault in Taiwan and the San Andreas Fault in California (Thomas et al., 2014; Gratier et al., 2011). The question that then remains is why would such a segment develop along this particular segment of the NAF and not elsewhere.

Finally, it is important to realize that all reports of aseismic slip published to date focused on the surroundings of the city of Ismetpasa, with the exception of Cetin et al. (2014) and Kaneko et al. (2012). At this peculiar location, as pointed out earlier by Aytun (1982), we observe vertical differential motion across the fault, consistent with subsidence measured north of the fault near Ismetpasa. Such subsidence is probably related to hydrological effects. Furthermore, this specific section is the only section where we observe slow slip events. Therefore, the slip behavior of the NAF in Ismetpasa is not representative of that of the entire creeping section.

All in all, it is difficult to conclude firmly on the rheology of fault material along this aseismic section. Aseismic slip seems steady, or slightly decaying, since at least the 1960's to the exception of the peculiar location of Ismetpasa. If further evidence of post-seismic slip following the 1944 earthquake were to be put forward, then an effective rate-strengthening rheology should be considered. In such case, slow slip events in Ismetpasa can be explained by the presence of small heterogeneities in frictional constitutive properties (Wei et al., 2013). Without any additional evidence, fault rheology is still a matter of debate as aseismic slip may result from a large nucleation size, geometrical complexities or low normal stress conditions. For instance, in the case of rate-weakening properties, reduced normal stress results in a large nucleation size hence promotes slow slip and spontaneous slow slip events may occur at the transition between locked and creeping regions (e.g. Liu & Rice, 2005).

6.3 A simple, testable explanation for shallow aseismic slip

Although the lack of evidence to constrain the rheology of fault material in this region might be disappointing, the geometry of the distribution of aseismic slip at depth may provide an explanation for the occurrence of shallow slip in this region. As shown by our model, the locking depth below the aseismic slip segment is shallower than elsewhere along the fault (Fig. 3). Such shallow locking depth is actually the only feature that differentiates the creeping segment from the rest of the fault covered by our study. This particular slip distribution is highlighted by the characteristic pattern of surface displacement rates, showing a gradual change in velocity approaching the fault (Fig. S-16 of supplementary materials). This bending, visible between 10 km away from the fault and the fault trace, is interpreted as the signature of elastic stress building up on a locked asperity. Since the fault slips at the surface, as highlighted by the step-like change in surface velocity across the fault, this locked asperity must be located between the locking depth and the bottom of the creeping zone.

Shallow locking depth results in higher stressing rates at the surface. For a semi-infinite dislocation embedded in an elastic halfspace buried at a depth d, shear stressing rate, $\dot{\tau}$, at the surface writes as $\dot{\tau} = \frac{\mu\dot{\delta}}{2\pi d}$ with μ the shear modulus and $\dot{\delta}$ the slip rate on the fault. Assuming a constant shear modulus and slip rates, shallowing the locking depth d from 20 to 10 km results in a twofold increase in stressing rate. For instance, with a 2 cm/yr slip rate and a 30 GPa shear modulus, shear stressing rate at the surface jumps from approximately 5 to 10 kPa/yr. Alone, such change in shear stressing rate should not lead to any change in slip behavior.

Whether shallow fault material is rate-weakening or -strengthening, the depth-distribution of effective normal stress, the difference between normal stress and pore pressure, influences frictional resistance. Low normal stress implies slip occurs at lower shear stress for a given coefficient of friction. Then, if shallow fault material is rate-strengthening, a higher (resp. lower) shear stressing rate should lead to the occurrence of constant shallow slow slip earlier (resp. later) in between two large earthquakes. If shallow fault material is rate-weakening, we must consider the depth-distribution of nucleation size.

Nucleation size is inversely proportional to normal stress (e.g. Ampuero & Rubin, 2008) and large nucleation size leads to conditionally stable slip. If the nucleation size is larger than the size of the fault, then slip cannot become dynamic and slip rates will remain slow. Effective normal stress results from the combination of overburden and pore pressure. To first order, normal stress increases linearly with depth, controlled by the density of crustal rocks. Considering the evolution of permeability with normal stress, it can be shown that effective normal stress increases with overburden until a depth of 3 to 5 km, depth below which normal stress is constant (Rice, 1992). There is therefore a lowering of normal stress at the surface and the depth distribution of normal stress results in a variation in nucleation size inversely proportional to depth, with maximum nucleation size at the surface. Considering such depth distribution of nucleation size is constant along strike, a local shallowing of the locking depth resulting in an increase in shear stressing rate at the surface would potentially increase slip rate at the surface while keeping slip to sub-dynamic speed (i.e. slow).

In both rate-strengthening or -weakening shallow fault material, a shallow (resp. deep) locking depth may result in faster (resp. slower) surface slip rates. In particular, such hypothesis does not involve any along strike variations of rheology or fluid content as only the shallowing of the locking depth is involved. Under these conditions, a homogeneous along strike fault rheology would be sufficient to explain spatial and temporal variations in surface aseismic slip rates. This hypothesis should now be evaluated carefully as other parameters may play a role, such as the constitutive parameters or the evolution of stresses in between two large earthquakes. Obviously, a physical explanation to a local variation in locking depth is unfortunately missing.

7 Conclusion

We provide 100 m-scale resolution time series of surface displacement across the North Anatolian Fault from Sentinel 1 InSAR data in order to explore the details of the spatial and temporal distribution of aseismic slip along the creeping section of Ismetpasa. We confirm the presence of aseismic slip over the shallow portion of the fault (surface to 5 km-depth), colocated with a shallow locking depth (10-12 km-depth). Our surface displacement data is elsewhere compatible with a 15-20 km locking depth. Current conclusions suggest that the evidence put forward to support the notion of long lasting afterslip following the 1944 earthquake are subject to debate, which, unfortunately, does not allow to conclude firmly on the rheology of the fault at shallow depth. Although our data cannot exclude a generic depth-dependent behavior of the relationship between slip rate and friction, the occurrence of slow slip events and the variability of rocks exposed at the surface forces to consider that rock type, hence constitutive properties, might not be the primary control on the presence of aseismic slip along this fault segment. Otherwise, one would need to consider the occurrence of shallow slow slip all along the fault, where large, $M_w > 7$ earthquakes have occurred over the 20th century and not only near Ismetpasa. We propose that shallow locking depth plays a role, although further investigation is needed to explain such particular feature.

Acknowledgments

The authors would like to thank Dr Harsha S. Bhat, Dr Cécile Lasserre, Pr. Pierre Dublanchet and Pr. Dmitry Garagash for insightful discussions. This project has received funding from the European Research Council (ERC) under the European Union's Horizon 2020 research and innovation program (Grant Agreements 758210 for project Geo4D). Romain Jolivet acknowledges funding from the Institut Universitaire de France. We thank the European Space Agency for the acquisition and the distribution of the SAR data by the Sentinel 1 constellation (may it fly forever and ever). InSAR data are available for download here: `https://peps.cnes.fr/`. ERA-Interim products are directly available for download at ECMWF (`https://www.ecmwf.int/`). InSAR data have been processed using the ISCE framework (`https://github.com/isce-framework/isce2`). Creepmeter data have been downloaded at the Unavco repository for geodetic data (`https://www.unavco.org/data/strain-seismic/creep-data/creep-data.html`). IGS data are available here `http://www.igs.org`. GNSS data from the Turkish national network are available

here: `https://www.tusaga-aktif.gov.tr/`. Data collected in the field with out stations along the North Anatolian Fault have been uploaded at `http://osf.io/9t3n7`. Modeling has been conducted using elements of the Classic Slip Inversion library (`https://github.com/jolivetr/csi`) and AlTar (`https://github.com/AlTarFramework/altar`). Notebooks detailing the procedure will be made available on Romain Jolivet's personal webpage.

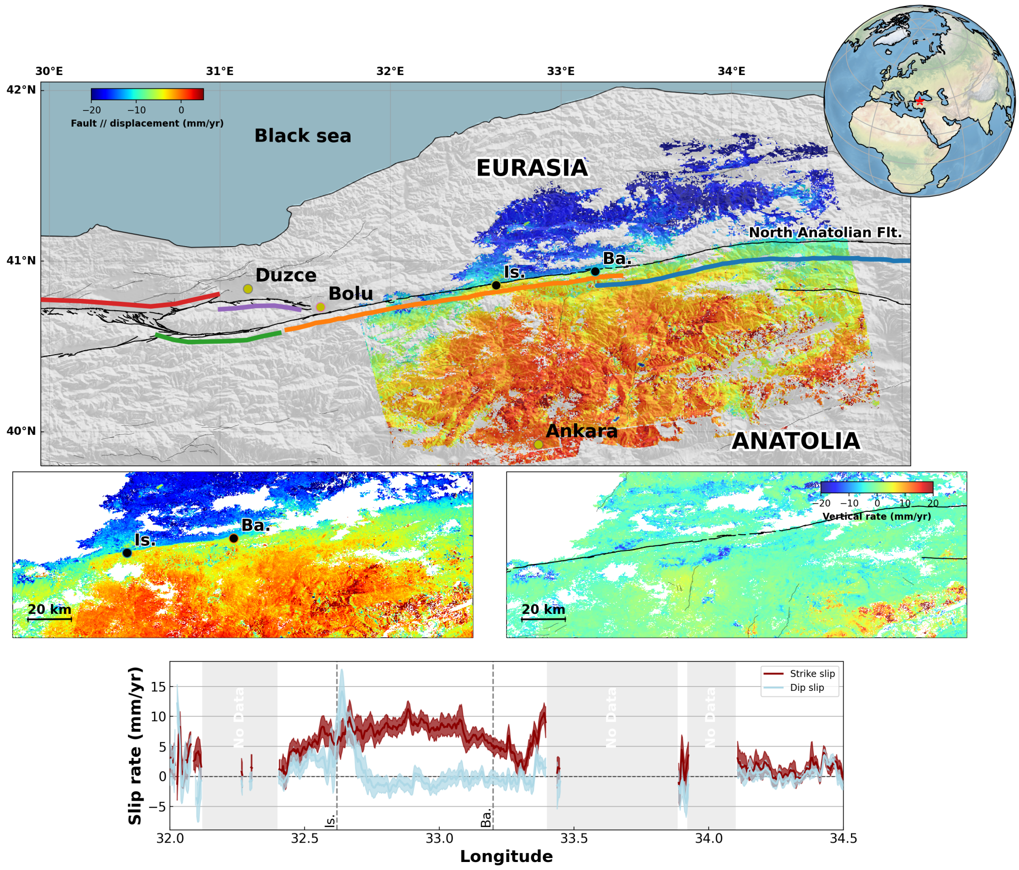

Figure 1. Fault parallel velocity map, vertical velocity map and surface slip - Top panel: Color indicates the fault parallel velocity derived from the combination of LOS velocity maps on Sentinel 1 ascending and descending tracks. Dark lines indicate the main trace of the North Anatolian Fault. Grey lines are secondary faults. Colored lines indicate the along strike extent of large historical and recent earthquakes including the 1943 M_w 7.6 Tosia-Ladik earthquake (blue), the 1944 M_w 7.3 Bolu-Gerede earthquake (orange), the 1967 M_w 7.2 Mudurnu earthquake (green), the 1999 M_w 7.6 Izmit earthquake (red) and the 1999 M_w 7.2 Dücze earthquake (purple). Center-left panel is a zoom on the area where aseismic slip is most visible, extending over the entire creeping section. Center-right panel shows the vertical displacement rate over that same area (positive is uplift). Lower panel shows surface slip rate along the fault as measured on the InSAR velocity maps. Red is strike slip while light blue is dip slip (i.e. effectively differential vertical motion at the fault trace). Grey shading shows areas of low coherence and data is missing. On all panels, Is. and Ba. indicate the location of the cities of Ismetpasa and Bayramoren, located at the end-points of the segment that slips aseismically.

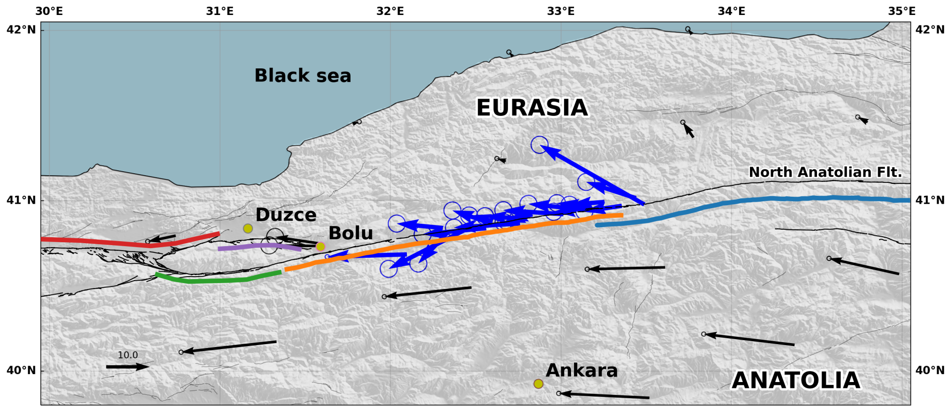

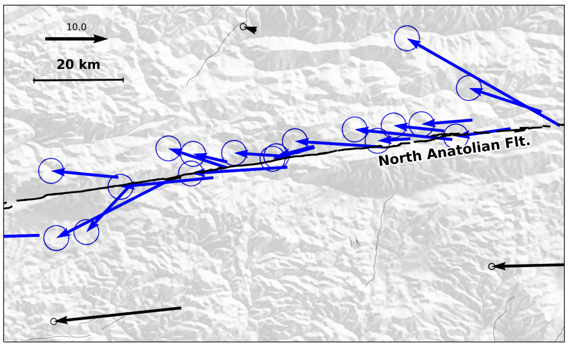

Figure 2. GNSS-derived velocities - Map of the GNSS-derived velocities from sites from the Turkish national network (in black) and from the Ismenet experiment (blue). A detailed description of the site setup for the Ismenet experiment as well as details of the data processing can be found in the supplementary information. Dark lines indicate the main North Anatolian fault. Gray lines are secondary faults. Colored lines indicate the along strike extent of large historical and recent earthquakes including the 1943 M_w 7.6 Tosia-Ladik earthquake (blue), the 1944 M_w 7.3 Bolu-Gerede earthquake (orange), the 1967 M_w 7.2 Mudurnu earthquake (green), the 1999 M_w 7.6 Izmit earthquake (red) and the 1999 M_w 7.2 Dücze earthquake (purple). Bottom panel is a close up on the region where aseismic slip has been identified. We see a clear change in measured velocities across the North Anatolian fault.

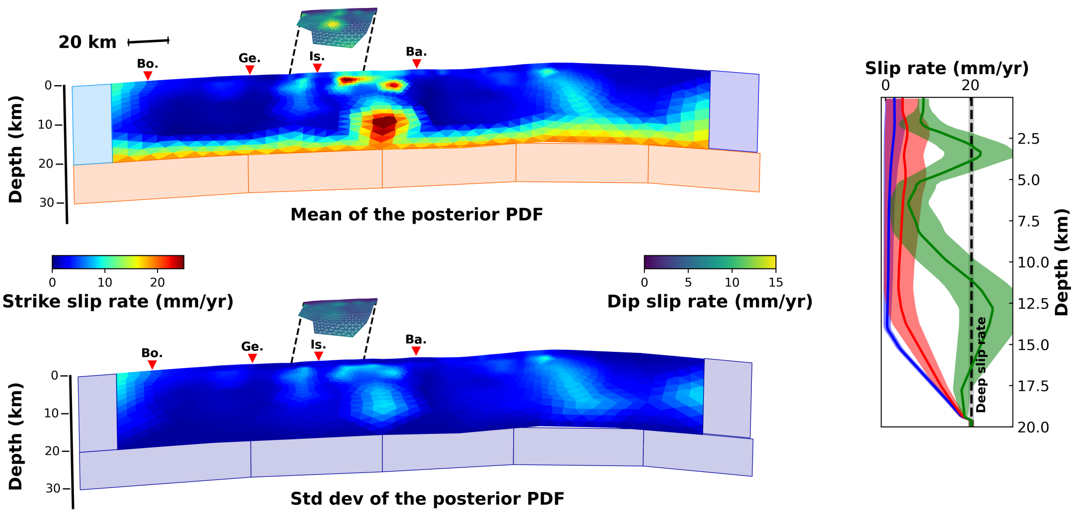

Figure 3. Fault slip distribution and uncertainties - Top: Mean of the posterior Probability Density Function of slip rate (strike slip). Rectangles on the side represent the dislocations used to model the western and eastern extension of the fault model as well as the deep dislocation modeling the far field displacement rate. Note that these dislocations extend sideways and at depth as semi-infinite structures. Small fault structure offset from the main fault shows the distribution of dip slip rate in the vicinity of the subsiding basin north of the city of Ismetpasa. Red triangles are cities located along the fault, including Bolu (Bo.), Gerede (Ge.), Ismetpasa (Is.) and Bayramoren (Ba.). **Bottom:** Standard deviation of the slip rate (strike slip and dip slip) posterior PDF. **Right:** Depth distribution of slip rate with associated uncertainties at longitude 31.9°E (blue), 32.9°E (green) and 33.9°E (red). Longitude 32.9°E is within the creeping section. Dark dashed line is the deep slip rate. The effective locking depth within the creeping section is inferred somewhere between 10 and 12.5 km depth.

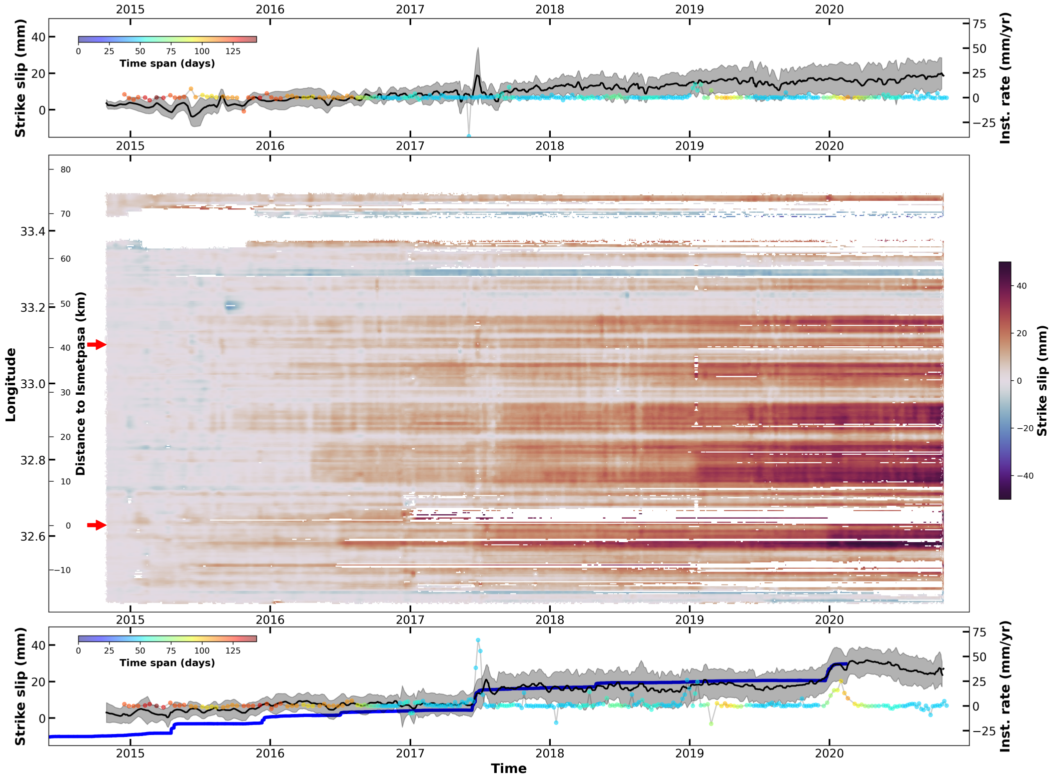

Figure 4. Time dependent surface slip rate - Space and time dependent surface slip rate (strike slip) obtained from regularly spaced profiles (see supp. mat.) Y-axis is labeled as a function on longitude and distance to Ismetpasa. Top and bottom plots show the time evolution of surface slip (dark) with the associated uncertainties (gray shading) at two distinct locations, including the Ismetpasa train station (bottom) and at 33.1°N (top). Both locations are indicated by red arrows on the main plot. Colored dots indicate the slip rate measured on sets of 9 consecutive acquisitions cleaned from atmospheric noise with a convolutional neural net (Rouet-Leduc et al., 2021). Color indicates the time span of the 9 acquisitions. Blue line is the strike slip measured by the creepmeter installed at the Ismetpasa train station Bilham et al. (2016).

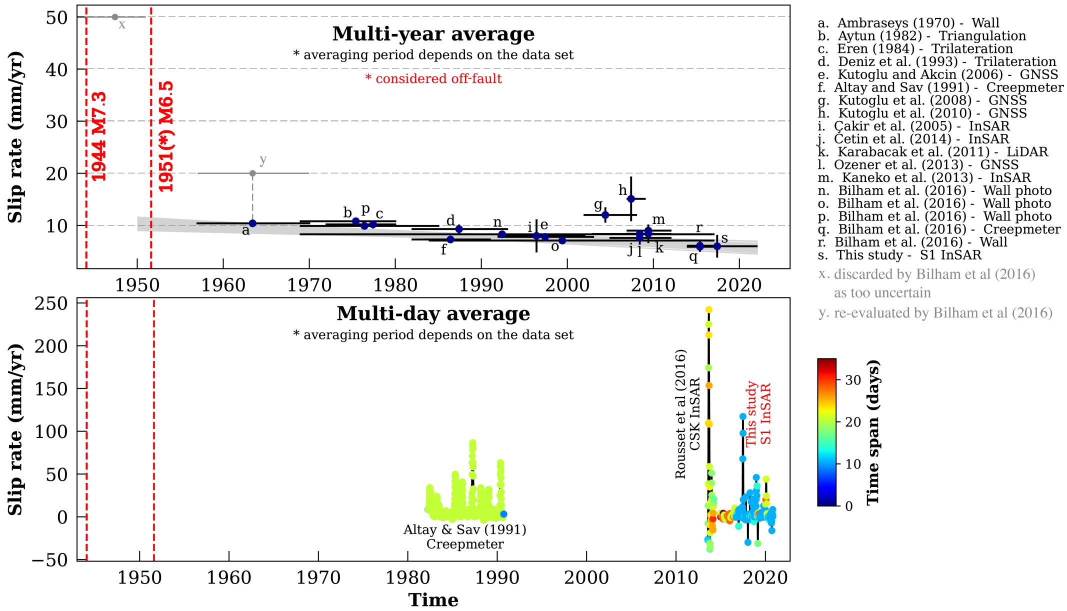

Figure 5. Evolution of surface aseismic slip rate at Ismetpasa - Surface slip rates averaged over several years (top) and over variable but day-to-week time scales (bottom). Colored dots indicate the time span over which slip rate has been estimated. Red dashed lines indicate the time of occurrence of the 1944 M_w 7.3 Bolu-Gerede and the 1951 M_w 6.5 Ismetpasa earthquakes. Gray shading indicates the range of possible models allowed from a Bayesian linear regression through the velocity estimates. Data are from Ambraseys (1970), Aytun (1982), Eren (1984), Deniz et al. (1993), Altay and Sav (1991), Çakir et al. (2005), Kutoglu and Akcin (2006), Kutoglu et al. (2008), Kutoglu et al. (2010), Karabacak et al. (2011), Deguchi (2011), Ozener et al. (2013) and Kaneko et al. (2012). Some rates were re-evaluated by Bilham et al. (2016). A table with the slip rates can be found in the supplementary informations.

References

Agram, P. S., Jolivet, R., Riel, B., Lin, Y. N., Simons, M., Hetland, E., ... Lasserre, C. (2013). New Radar Interferometric Time Series Analysis Toolbox Released. *Eos*, *94* (7), 69–76. doi: 10.1029/2011JB008731

Altamimi, Z., Rebischung, P., Métivier, L., & Collilieux, X. (2016). ITRF2014: A new release of the International Terrestrial Reference Frame modeling nonlinear station motions. *Journal of Geophysical Research: Solid Earth*, *121* (8), 6109–6131. doi: 10.1002/2016JB013098

Altay, C., & Sav, H. (1991). Continuous creep measurement along the North Anatolian Fault zone. *Bulletin of the geological congres of Turkey*, *6*, 77–84.

Ambraseys, N. N. (1970). Some characteristic features of the Anatolian fault zone. *Tectonophysics*, *9*, 143–165.

Ampuero, J.-P., & Rubin, A. M. (2008). Earthquake nucleation on rate and state faults – Aging and slip laws. *Journal of Geophysical Research*, *113* (B1), B01302–21. doi: 10.1029/2007JB005082

Avouac, J.-P. (2015). From Geodetic Imaging of Seismic and Aseismic Fault Slip to Dynamic Modeling of the Seismic Cycle. *Annual Review of Earth and Planetary Sciences*, *43* (1), 233–271. doi: 10.1146/annurev-earth-060614-105302

Aytun, A. (1982). Creep Measurements in the Ismetpaşa Region of the North Anatolian Fault Zone. *Multidisciplinary Approach to Earthquake Prediction Progress in Earthquake Prediction Research*, *2*, 279–292.

Barbot, S., & Weiss, J. R. (2021). Connecting subduction, extension, and shear localization across the aegean sea and anatolia. *Geophysical Journal International*, *226* (1), 422-445. doi: 10.1093/gji/ggab078

Barka, A. (1996). Slip distribution along the north anatolian fault associated with the large earthquakes of the period 1939 to 1967. *Bulletin of the Seismological Society of America*, *86* (5), 1238–1254.

Benoit, A., Pinel-Puyssegur, B., Jolivet, R., & Lasserre, C. (2020). CorPhU: an algorithm based on phase closure for the correction of unwrapping errors in SAR interferometry. *Geophysical Journal International*, *221* (3), 1959–1970. doi: 10.1093/gji/ggaa120

Bevis, M., & Brown, A. (2014). Trajectory models and reference frames for crustal motion geodesy. *Journal of Geodesy*, *88* (3), 283–311. doi: 10.1007/s00190-013

-0685-5

Bilham, R., Ozener, H., Mencin, D., Dogru, A., Ergintav, S., Çakir, Z., ... Mattioli, G. (2016). Surface creep on the North Anatolian Fault at Ismetpasa, Turkey, 1944-2016. *Journal of Geophysical Research-Solid Earth*, *121*, 7409– 7431. doi: 10.1002/2016JB013394

Blanpied, M. L., Lockner, D. A., & Byerlee, J. D. (1991). Fault stability inferred from granite sliding experiments at hydrothermal conditions. *Geophysical Research Letters*, *18*(4), 609–612. doi: 10.1029/91GL00469

Bletery, Q., Cavalié, O., Nocquet, J.-M., & Ragon, T. (2020). Distribution of interseismic coupling along the north and east anatolian faults inferred from insar and gps data. *Geophysical Research Letters*, *47*(16), e2020GL087775. doi: 10.1029/2020GL087775

Bouchon, M., Karabulut, H., Aktar, M., Ozalaybey, S., Schmittbuhl, J., & Bouin, M. P. (2011). Extended Nucleation of the 1999 Mw 7.6 Izmit Earthquake. *Science*, *331*(6019), 877–880. doi: 10.1126/science.1197341

Bürgmann, R. (2018). The geophysics, geology and mechanics of slow fault slip. *Earth and Planetary Science Letters*, *495*, 112–134. doi: 10.1016/j.epsl.2018.04.062

Çakir, Z., Akoglu, A., Belabbes, S., Ergintav, S., & Meghraoui, M. (2005). Creeping along the Ismetpasa section of the North Anatolian fault (Western Turkey): Rate and extent from InSAR. *Earth and Planetary Science Letters*, *238*(1-2), 225–234. doi: 10.1016/j.epsl.2005.06.044

Candela, T., Renard, F., Klinger, Y., Mair, K., Schmittbuhl, J., & Brodsky, E. E. (2012). Roughness of fault surfaces over nine decades of length scales. *Journal of Geophysical Research*, *117*(B8), B08409. doi: 10.1029/2011JB009041

Cattania, C., & Segall, P. (2021). Precursory slow slip and foreshocks on rough faults. *Journal of Geophysical Research: Solid Earth*, *126*(4), e2020JB020430. doi: 10.1029/2020JB020430

Cetin, E., Cakir, Z., Meghraoui, M., Ergintav, S., & Akoglu, A. M. (2014). Extent and distribution of aseismic slip on the Ismetpaşa segment of the North Anatolian Fault (Turkey) from Persistent Scatterer InSAR. *Geochemistry Geophysics Geosystems*, *15*(7), 2883–2894. doi: 10.1002/2014GC005307

Dalaison, M., & Jolivet, R. (2020). A kalman filter time series analysis method for insar. *Journal of Geophysical Research: Solid Earth*, *125*(7), e2019JB019150. doi: 10.1029/2019JB019150

Dalaison, M., Jolivet, R., & Le Pourhiet, L. (2023). A snapshot of the long-term evolution of a distributed tectonic plate boundary [doi: 10.1126/sciadv.add7235]. *Science Advances*, *9*(16), eadd7235. Retrieved from `https://doi.org/10.1126/sciadv.add7235` doi: 10.1126/sciadv.add7235

Dalaison, M., Jolivet, R., van Rijsingen, E. M., & Michel, S. (2021). The interplay between seismic and aseismic slip along the chaman fault illuminated by insar. *Journal of Geophysical Research: Solid Earth*, *126*(12), e2021JB021935. doi: 10.1029/2021JB021935

Deguchi. (2011). Detection of fault creep around naf by insar time series analysis using palsar data. *Proc. of SPIE, SAR Image Analysis, Modeling, and Techniques XI*, *8179*. doi: 10.1117/12.898478

DeMets, C., Gordon, R. G., & Argus, D. F. (2010). Geologically current plate motions. *Geophysical Journal International*, *181*(1), 1–80. doi: 10.1111/j.1365-246X.2009.04491.x

den Hartog, S. A. M., & Spiers, C. J. (2013). Influence of subduction zone conditions and gouge composition on frictional slip stability of megathrust faults. *Tectonophysics*, *600*, 75–90. doi: 10.1016/j.tecto.2012.11.006

Deniz, R., Aksoy, A., Yalin, D., Seeger, H., Franke, P., Hirsch, O., & Bautsch, P. (1993). Determination of crustal movements in turkey by terrestrial geodetic methods. *Journal of Geodynamics*, *18*(1), 13–22. doi: 10.1016/0264-3707(93)90024-Z

Dettmer, J., Benavente, R., Cummins, P. R., & Sambridge, M. (2014). Trans-dimensional finite-fault inversion. *Geophysical Journal International*, *199*(2), 735–751. doi: 10.1093/gji/ggu280

Dianala, J. D. B., Jolivet, R., Thomas, M. Y., Fukushima, Y., Parsons, B., & Walker, R. (2020). The relationship between seismic and aseismic slip on the philippine fault on leyte island: Bayesian modeling of fault slip and geothermal subsidence. *Journal of Geophysical Research: Solid Earth*, *125*(12), e2020JB020052. doi: 10.1029/2020JB020052

Dragert, H., Wang, K., & Thomas, J. S. (2001). A Silent Slip Event on the Deeper Cascadia Subduction Interface. *Science*, *292*(5521), 1525–1528. doi: 10.1126/

science.1060152

Duputel, Z., Agram, P. S., Simons, M., Minson, S. E., & Beck, J. L. (2014). Accounting for prediction uncertainty when inferring subsurface fault slip. *Geophysical Journal International*, *197*(1), 464–482. doi: 10.1093/gji/ggt517

Duquesnoy, T., Barrier, E., Kasser, M., Aurelio, M., Gaulon, R., Punongbayan, R. S., & Rangin, C. (1994). Detection of creep along the Philippine fault: First results of geodetic measurements on Leyte island, central Philippine. *Geophysical Research Letters*, *21*(11), 975–978. doi: 10.1029/94GL00640

Ellsworth, W. L., & Bulut, F. (2018). Nucleation of the 1999 Izmit earthquake by a triggered cascade of foreshocks. *Nature Geoscience*, *84*, 1–6. doi: 10.1038/s41561-018-0145-1

Eren, K. (1984). Strain analysis along the north analtolian fault by using geodetic surveys. *Bulletin géodésique*, *58*(2), 137–150. doi: 10.1007/BF02520898

Fattahi, H., Agram, P., & Simons, M. (2016). A Network-Based Enhanced Spectral Diversity Approach for TOPS Time-Series Analysis. *IEEE Transactions on Geoscience and Remote Sensing*, *55*(2), 777-786. doi: 10.1109/TGRS.2016.2614925

Goldstein, R. M., & Werner, C. L. (1998, November). Radar interferogram filtering for geophysical applications. *Geophysical Research Letters*, *25*(21), 4035–4038.

Goldstein, R. M., Zebker, H. A., & Werner, C. L. (1988). Satellite radar interferometry: Two-dimensional phase unwrapping. *Radio Science*, *23*(4), 713–720.

Gratier, J. P., Richard, J., Renard, F., Mittempergher, S., Doan, M. L., Di Toro, G., ... Boullier, A. M. (2011). Aseismic sliding of active faults by pressure solution creep: Evidence from the San Andreas Fault Observatory at Depth. *Geology*, *39*(12), 1131–1134. doi: 10.1130/G32073.1

Gurrola, E., Rosen, P., Sacco, G., Seliga, W., Zebker, H., Simons, M., & Sandwell, D. (2010). Sar scientific computing environment. In *Paper presented at the american geophysical union fall meeting, san francisco, ca.*

Herring, T. A., Floyd, M., King, R., & McClusky, S. C. (2015). Globk reference manual, global kalman filter vlbi and gps analysis program, release 10.6. (Computer software manual No. June). Cambridge, MA, USA. Retrieved from `https://geoweb.mit.edu/gg`

Herring, T. A., King, R., Floyd, M., & McClusky, S. C. (2018). Introduction to gamit/globk, release 10.7. (Computer software manual No. June). Cambridge, MA, USA. Retrieved from https://geoweb.mit.edu/gg

Jolivet, R., Agram, P. S., Lin, N. Y., Simons, M., Doin, M.-P., Peltzer, G., & Li, Z. (2014). Improving InSAR geodesy using Global Atmospheric Models. *Journal of Geophysical Research-Solid Earth*, *119*(3), 2324–2341. doi: 10.1002/2013JB010588

Jolivet, R., Candela, T., Lasserre, C., Renard, F., Klinger, Y., & Doin, M. P. (2015). The Burst-Like Behavior of Aseismic Slip on a Rough Fault: The Creeping Section of the Haiyuan Fault, China. *Bulletin of the Seismological Society of America*, *105*(1), 480–488. doi: 10.1785/0120140237

Jolivet, R., & Frank, W. B. (2020). The Transient and Intermittent Nature of Slow Slip. *AGU Advances*, *1*(1), e2019AV000126–8. doi: 10.1029/2019AV000126

Jolivet, R., Grandin, R., Lasserre, C., Doin, M. P., & Peltzer, G. (2011). Systematic insar tropospheric phase delay corrections from global meteorological reanalysis data. *Geophysical Research Letters*, *38*(17). doi: 10.1029/2011GL048757

Jolivet, R., Simons, M., Agram, P. S., Duputel, Z., & Shen, Z. K. (2015). Aseismic slip and seismogenic coupling along the central San Andreas Fault. *Geophysical Research Letters*, *42*(2), 297–306. doi: 10.1002/2014GL062222

Kaduri, M., Gratier, J.-P., Lasserre, C., Çakir, Z., & Renard, F. (2019). Quantifying the partition between seismic and aseismic deformation along creeping and locked sections of the north anatolian fault, turkey. *Pure and Applied Geophysics*, *176*(3), 1293–1321. doi: 10.1007/s00024-018-2027-2

Kaneko, Y., Avouac, J.-P., & Lapusta, N. (2010). Towards inferring earthquake patterns from geodetic observations of interseismic coupling. *Nature Geoscience*, *3*(5), 363–369. doi: 10.1038/ngeo843

Kaneko, Y., Fialko, Y., Sandwell, D. T., Tong, X., & Furuya, M. (2012). Interseismic deformation and creep along the central section of the North Anatolian fault (Turkey): InSAR observations and implications for rate-and-state friction properties. *Journal of Geophysical Research-Solid Earth*, *118*, 316– 331. doi: 10.1029/2012JB009661

Karabacak, V., Altunel, E., & Cakir, Z. (2011). Monitoring aseismic surface creep along the north anatolian fault (turkey) using ground-based lidar. *Earth and Planetary Science Letters*, *304*(1), 64–70. doi: 10.1016/j.epsl.2011.01.017

Khoshmanesh, M., & Shirzaei, M. (2018). Multiscale Dynamics of Aseismic Slip on Central San Andreas Fault. *Geophysical Research Letters*, *45*(5), 2274–2282. doi: 10.1002/2018GL077017

Kodaira, S., Iidaka, T., Kato, A., Park, J.-O., Iwasaki, T., & Kaneda, Y. (2004). High pore fluid pressure may cause silent slip in the nankai trough. *Science*, *304*(5675), 1295–1298. doi: 10.1126/science.1096535

Kondo, H., Awata, Y., Emre, Ö., Doġan, A., Özalp, S., Tokay, F., … Okumura, K. (2005). Slip distribution, fault geometry, and fault segmentation of the 1944 bolu-gerede earthquake rupture, north anatolian fault, turkey. *Bulletin of the Seismological Society of America*, *95*(4), 1234–1249. doi: 10.1785/0120040194

Kondo, H., Özaksoy, V., & Yıldirim, C. (2010). Slip history of the 1944 bolu-gerede earthquake rupture along the north anatolian fault system: Implications for recurrence behavior of multisegment earthquakes. *Journal of Geophysical Research: Solid Earth*, *115*(B4). doi: 10.1029/2009JB006413

Kutoglu, H. S., & Akcin, H. (2006). Determination of the 30-year creep trend on the ismetpaşa segment of the north anatolian fault using an old geodetic network. *Earth, Planets and Space*, *58*(8), 937–942. doi: 10.1186/BF03352598

Kutoglu, H. S., Akcin, H., Gundogdu, O., Gormus, K. S., & Koksal, E. (2010, 12). Relaxation on the ismetpasa segment of the north anatolian fault after the golcuk $m_w = 7.4$ and duzce $m_w = 7.2$ shocks. *Nat. Hazards Earth Syst. Sci.*, *10*(12), 2653–2657. doi: 10.5194/nhess-10-2653-2010

Kutoglu, H. S., Akcin, H., Kemaldere, H., & Gormus, K. S. (2008, 12). Triggered creep rate on the ismetpasa segment of the north anatolian fault. *Nat. Hazards Earth Syst. Sci.*, *8*(6), 1369–1373. doi: 10.5194/nhess-8-1369-2008

Liu, Y., & Rice, J. R. (2005). Aseismic slip transients emerge spontaneously in three-dimensional rate and state modeling of subduction earthquake sequences. *Journal of Geophysical Research: Solid Earth (1978–2012)*, *110*(B8), 609–14. doi: 10.1029/2004JB003424

Lohman, R. B., & Simons, M. (2005). Some thoughts on the use of InSAR data to constrain models of surface deformation: Noise structure and data downsampling. *Geochemistry, Geophysics, Geosystem*, *6*(1), Q01007. doi: 10.1029/2004GC000841

Maurer, J., & Johnson, K. (2014). Fault coupling and potential for earthquakes on the creeping section of the central San Andreas Fault. *Journal of Geophysical Research*, *119*(5), 2013JB010741–4428. doi: 10.1002/2013JB010741

Mazzotti, S., Le Pichon, X., Henry, P., & Miyazaki, S.-I. (2000). Full interseismic locking of the Nankai and Japan-west Kurile subduction zones: An analysis of uniform elastic strain accumulation in Japan constrained by permanent GPS. *Journal of Geophysical Research: Solid Earth (1978–2012)*, *105*(B6), 13159–13177. doi: 10.1029/2000JB900060

Minson, S. E., Simons, M., & Beck, J. L. (2013). Bayesian inversion for finite fault earthquake source models I–theory and algorithm. *Geophysical Journal International*, *194*(3), 1701–1726. doi: 10.1093/gji/ggt180

Mogi, K. (1958). Relations between the Eruptions of Various Volcanoes and the Deformation of the Ground Surface around them. *Bulleting of the Earthquake Research Institute*, *36*, 99–134.

Moreno, M., Haberland, C., Oncken, O., Rietbrock, A., Angiboust, S., & Heidbach, O. (2014). Locking of the chile subduction zone controlled by fluid pressure before the 2010 earthquake. *Nature Geoscience*, *7*(4), 292–296. doi: 10.1038/ngeo2102

Nocquet, J.-M. (2018a). *Pyacs: A set of python tools for gps analysis and tectonic modelling.* 19th General Assembly of Wegener.

Nocquet, J.-M. (2018b). Stochastic static fault slip inversion from geodetic data with non-negativity and bound constraints. *Geophysical Journal International*, *214*(1), 366–385. doi: 10.1093/gji/ggy146

Ozener, H., Dogru, A., & Turgut, B. (2013). Quantifying aseismic creep on the ismetpasa segment of the north anatolian fault zone (turkey) by 6 years of gps observations. *Journal of Geodynamics*, *67*, 72–77. doi: 10.1016/j.jog.2012.08.002

Reid, H. F. (1911). The elastic rebound theory of earthquakes. *Univ. Calif. Publ. Bull. Dept. Geol.*, *6*, 413–444.

Rice, J. R. (1992). Fault stress states, pore pressure distributions, and the weakness of the san andreas fault. In B. Evans & T.-F. Wong (Eds.), *Fault mechanics and transport properties in rocks* (p. 475-503). Academic Press.

Romanet, P., Bhat, H. S., Jolivet, R., & Madariaga, R. (2018). Fast and Slow Slip Events Emerge Due to Fault Geometrical Complexity. *Geophysical Research*

Letters, *45*(10), 4809–4819. doi: 10.1029/2018GL077579

Rouet-Leduc, B., Jolivet, R., Dalaison, M., Johnson, P. A., & Hulbert, C. (2021). Autonomous extraction of millimeter-scale deformation in insar time series using deep learning. *Nature Communications*, *12*(1), 6480. doi: 10.1038/s41467-021-26254-3

Rousset, B., Jolivet, R., Simons, M., Lasserre, C., Riel, B., Milillo, P., ... Renard, F. (2016). An aseismic slip transient on the North Anatolian Fault. *Geophysical Research Letters*, *43*(7), 3254–3262. doi: 10.1002/2016GL068250

Ruiz, S., Metois, M., Fuenzalida, A., Ruiz, J., Leyton, F., Grandin, R., ... Campos, J. (2014). Intense foreshocks and a slow slip event preceded the 2014 Iquique Mw 8.1 earthquake. *Science*, *345*(6201), 1165–1169. doi: 10.1126/science.1256074

Ryder, I., & Bürgmann, R. (2008, December). Spatial variations in slip deficit on the central San Andreas Fault from InSAR. *Geophysical Journal International*, *175*(3), 837–852. doi: 10.1111/j.1365-246X.2008.03938.x

Savage, J. C., & Burford, R. O. (1973). Geodetic determination of relative plate motion in central California. *Journal of Geophysical Research*, *78*(5), 832–845. doi: 10.1029/JB078i005p00832

Scholz, C. H. (1998). Earthquakes and friction laws. *Nature*, *391*(6662), 37–42. doi: 10.1038/34097

Socquet, A., Valdes, J. P., Jara, J., Cotton, F., Walpersdorf, A., Cotte, N., ... Norabuena, E. (2017). An 8 month slow slip event triggers progressive nucleation of the 2014 Chile megathrust. *Geophysical Research Letters*, *44*(9), 4046–4053. doi: 10.1002/2017GL073023

Steinbrugge, K. V., Zacher, E. G., Tocher, D., Whitten, C. A., & Claire, C. N. (1960). Creep on the San Andreas fault. *Bulletin of the Seismological Society of America*, *50*(3), 389–415.

Sudhaus, H., & Jónsson, S. (2009). Improved source modelling through combined use of InSAR and GPS under consideration of correlated data errors: application to the June 2000 Kleifarvatn earthquake, Iceland. *Geophysical Journal International*, *176*(2), 389–404. doi: 10.1111/j.1365-246X.2008.03989.x

Thomas, M. Y., Avouac, J.-P., Gratier, J.-P., & Lee, J.-C. (2014). Lithological control on the deformation mechanism and the mode of fault slip on the Longitudinal Valley Fault, Taiwan. *Tectonophysics*, *632*, 1–16. doi: 10.1016/j.tecto.2014.05.038

Thomas, M. Y., Avouac, J.-P., & Lapusta, N. (2017). Rate-and-state friction properties of the Longitudinal Valley Fault from kinematic and dynamic modeling of seismic and aseismic slip. *Journal of Geophysical Research-Solid Earth*, *122*(4), 3115–3137. doi: 10.1002/2016JB013615

Wallace, L. M. (2020). Slow slip events in new zealand. *Annual Review of Earth and Planetary Sciences*, *48*(1), 175–203. doi: 10.1146/annurev-earth-071719-055104

Wei, M., Kaneko, Y., Liu, Y., & McGuire, J. J. (2013). Episodic fault creep events in California controlled by shallow frictional heterogeneity. *Nature Geoscience*, *6*, 566–570. doi: 10.1038/ngeo1835

Weiss, J. R., Walters, R. J., Morishita, Y., Wright, T. J., Lazecky, M., Wang, H., … Parsons, B. (2020, 11). High-resolution surface velocities and strain for anatolia from sentinel-1 insar and gnss data. *Geophysical Research Letters*, *47*(17), e2020GL087376. doi: 10.1029/2020GL087376

Williams, S. D. P. (2003). The effect of coloured noise on the uncertainties of rates estimated from geodetic time series. *Journal of Geodesy*, *76*(9-10), 483–494. doi: 10.1007/s00190-002-0283-4

Supplementary Materials

Daily to centennial behavior of aseismic slip along the central section of the North Anatolian Fault

R. Jolivet[1,2], J. Jara[1], M. Dalaison[1], B. Rouet-Leduc[3], A. Özdemir[4], U. Dogan[4], Z. Çakir[5], S. Ergintav[6]& P. Dubernet[1]

[1]Laboratoire de Géologie, Département de Géosciences, École Normale Supérieure, PSL Université, CNRS UMR 8538, Paris, France
[2]Institut Universitaire de France, 1 rue Descartes, 75006 Paris
[3]Disaster Prevention Research Institute, Kyoto University, Kyoto, Japan
[4] Department of Geomatic Engineering, Yildiz Technical University, 34220 Istanbul, Turkey
[5]Department of Geology, Istanbul Technical University, 34469 Istanbul, Turkey
[6]Department of Geodesy, Kandilli Observatory and Earthquake Research Institute, Bogazici University, 34684 Istanbul, Turkey

Corresponding author: Romain Jolivet, romain.jolivet@ens.fr

1 InSAR data complementary figures

1.1 InSAR dataset

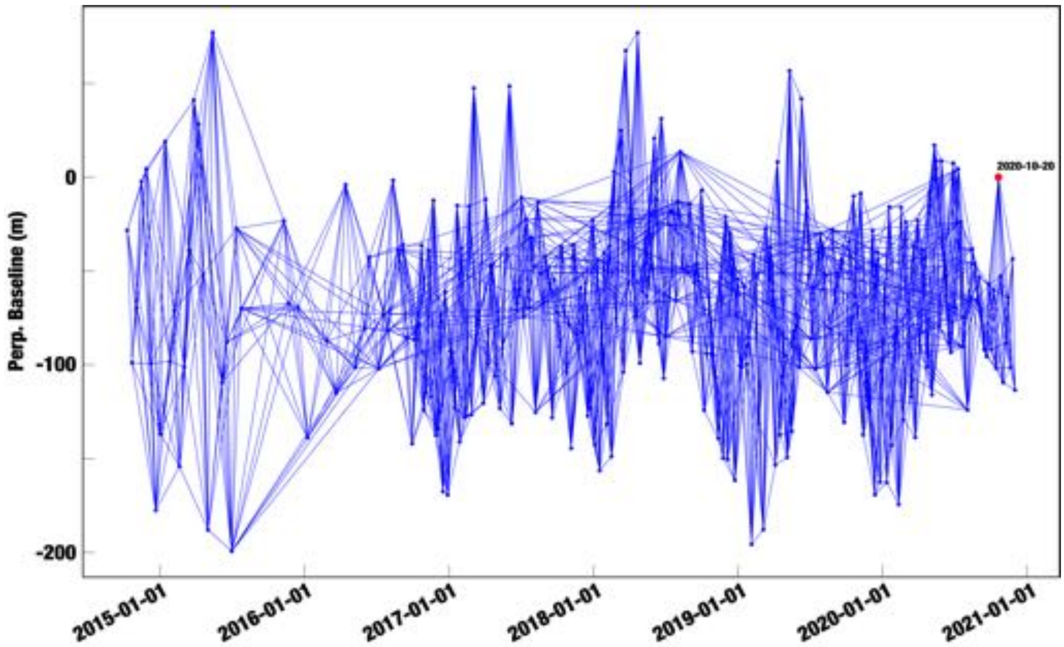

Figure S-1: **Perpendicular baseline as a function of acquisition dates for track 65 -** Blue dots represent the perpendicular baseline at the date of each acquisition by the Sentinel 1 A and B satellites. Red dot is the image chosen as reference for the geometry. Blue lines are the interferograms we computed.

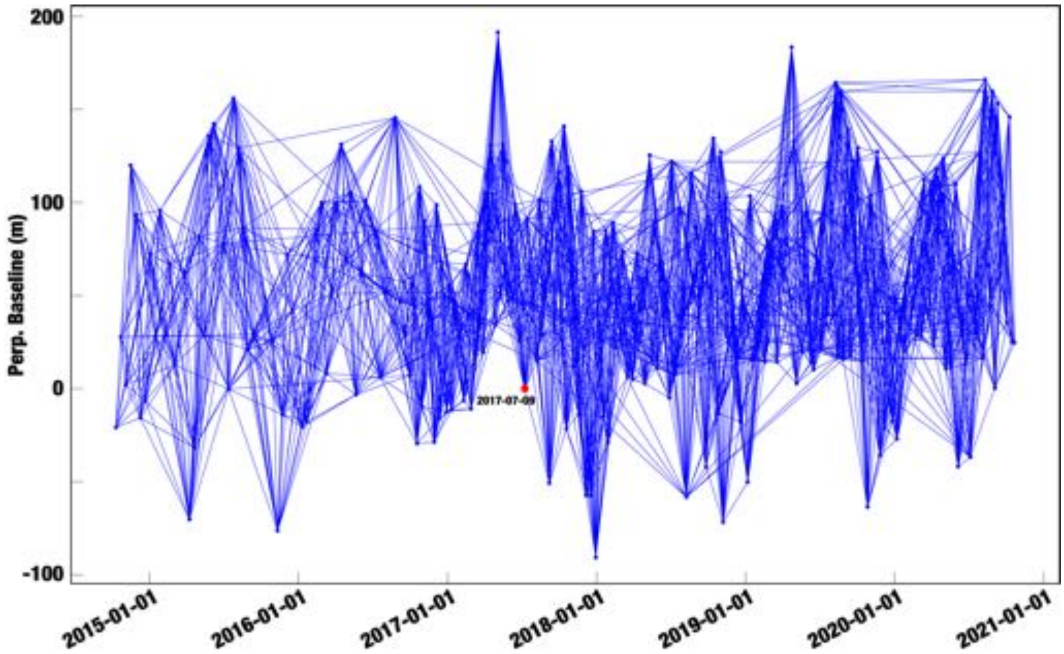

Figure S-2: **Perpendicular baseline as a function of acquisition dates for track 87 -** Blue dots represent the perpendicular baseline at the date of each acquisition by the Sentinel 1 A and B satellites. Red dot is the image chosen as reference for the geometry. Blue lines are the interferograms we computed.

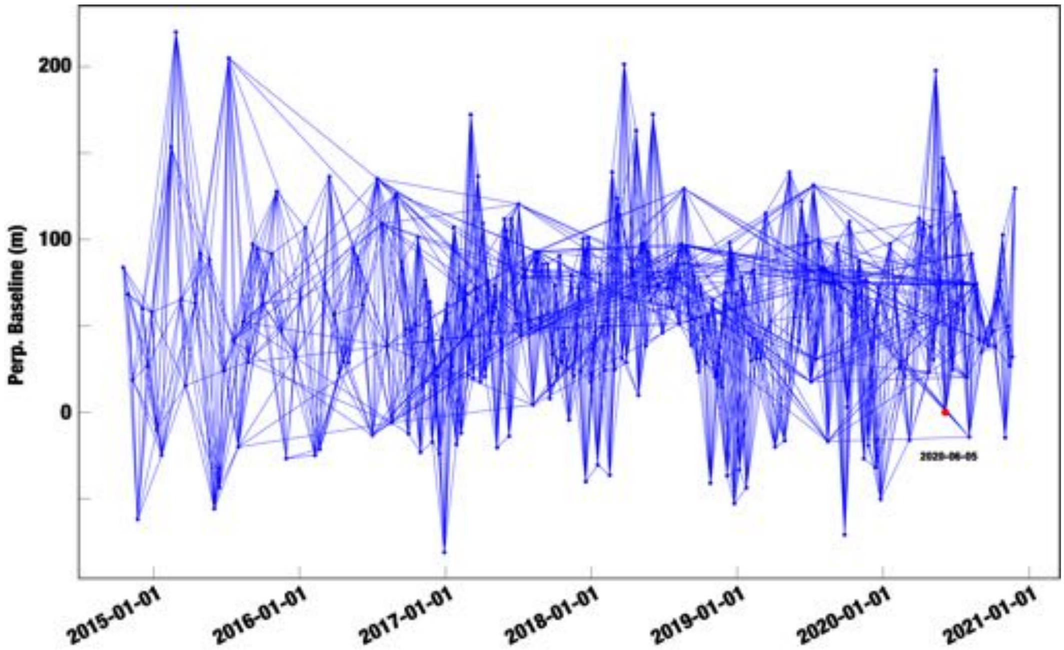

Figure S-3: **Perpendicular baseline as a function of acquisition dates for track 167-** Blue dots represent the perpendicular baseline at the date of each acquisition by the Sentinel 1 A and B satellites. Red dot is the image chosen as reference for the geometry. Blue lines are the interferograms we computed.

1.2 Full velocity maps

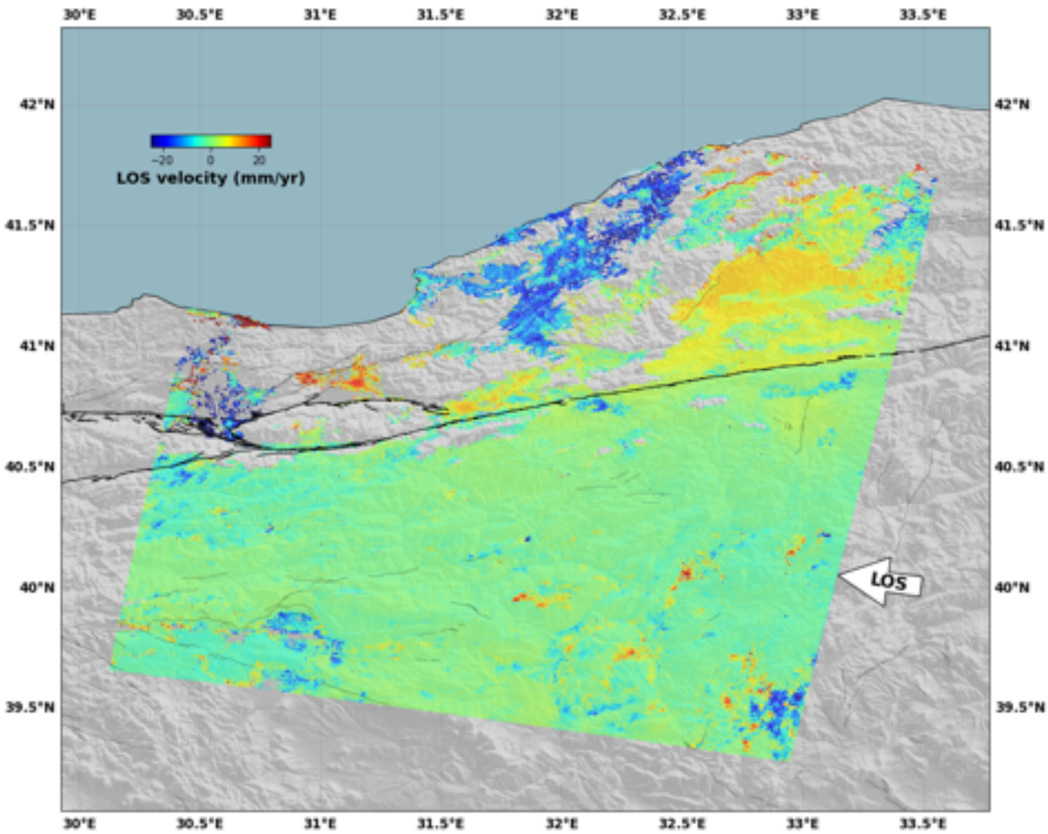

Figure S-4: **Line-of-sight velocity map from track 65 -** Velocity map computed from the time series of InSAR data on track 65. All available pixels are shown.

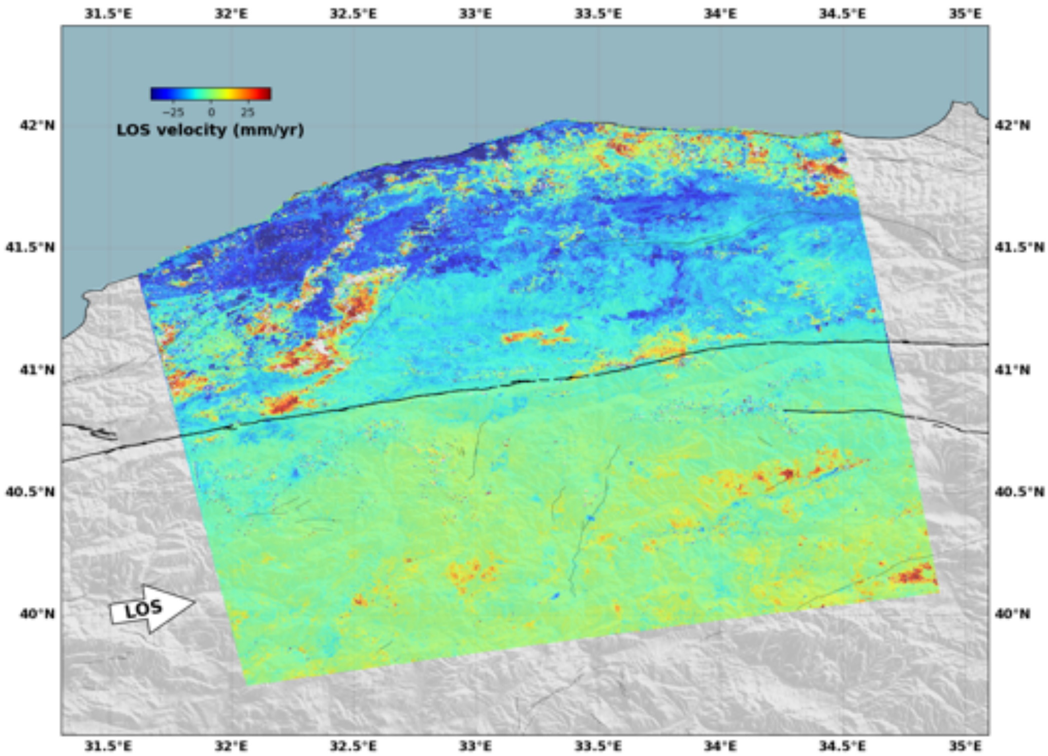

Figure S-5: **Line-of-sight velocity map from track 87 -** Velocity map computed from the time series of InSAR data on track 87. All available pixels are shown.

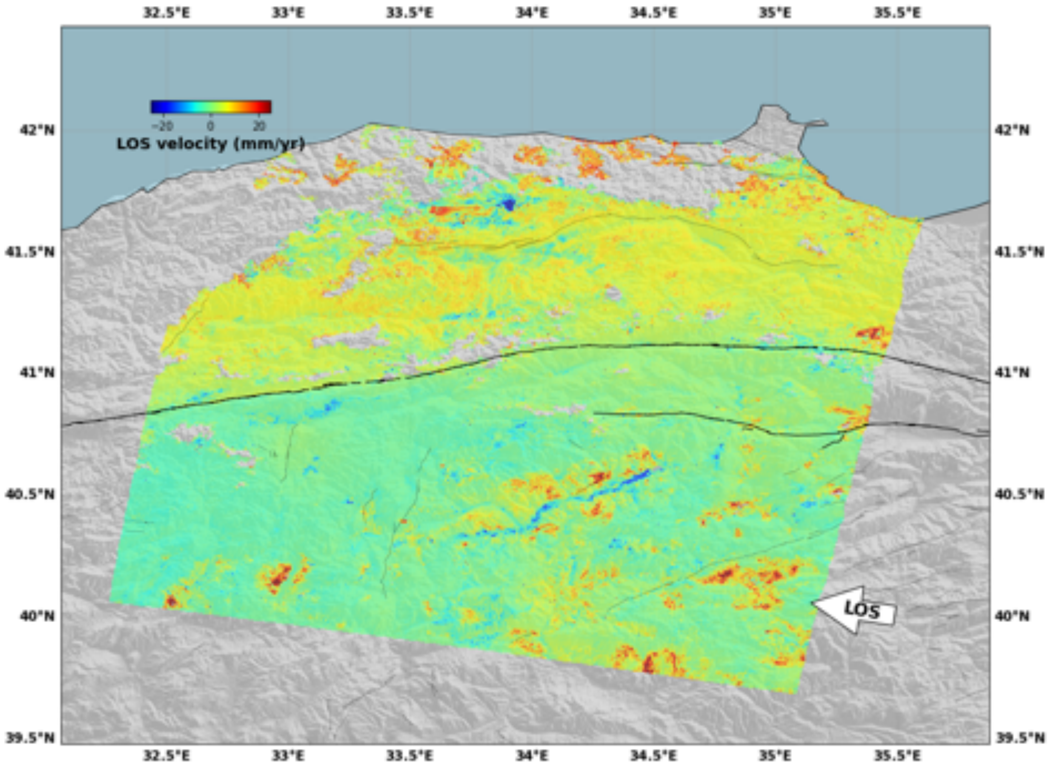

Figure S-6: **Line-of-sight velocity map from track 167 -** Velocity map computed from the time series of InSAR data on track 167. All available pixels are shown.

1.3 Velocity standard deviation maps

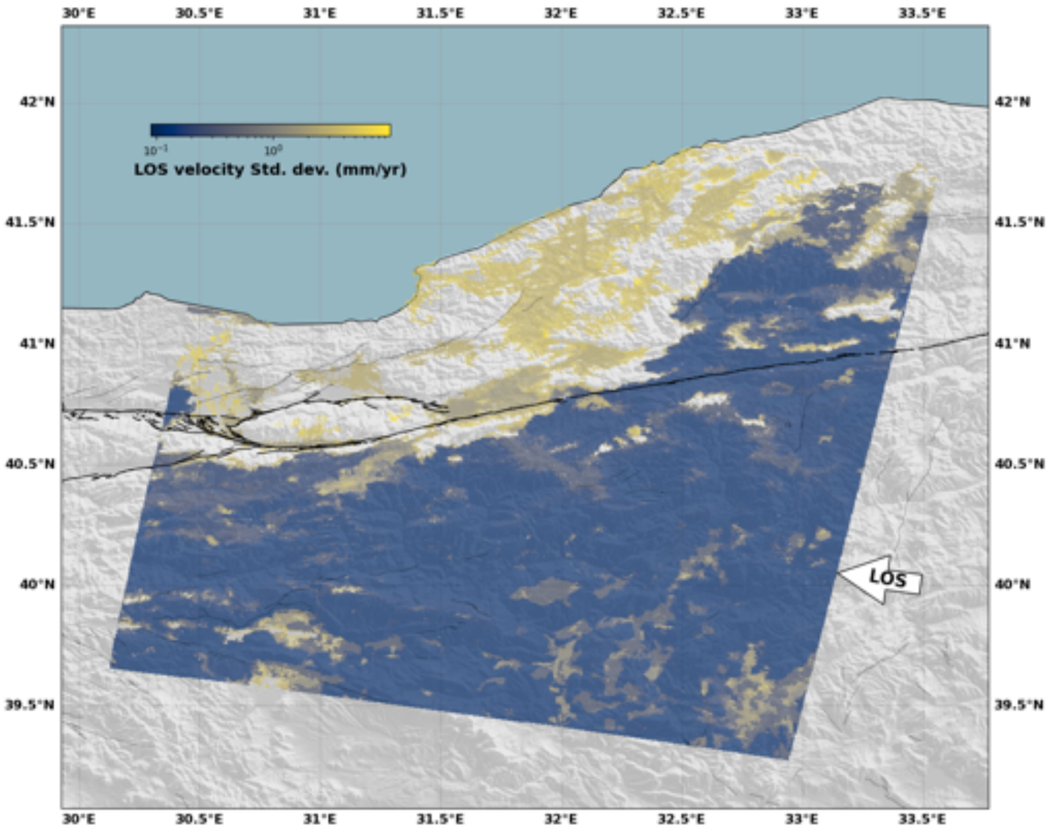

Figure S-7: **Line-of-sight velocity standard deviation map from track 65 -** Standard deviations are from the analyzed state covariance at the end of the Kalman filtering procedure.

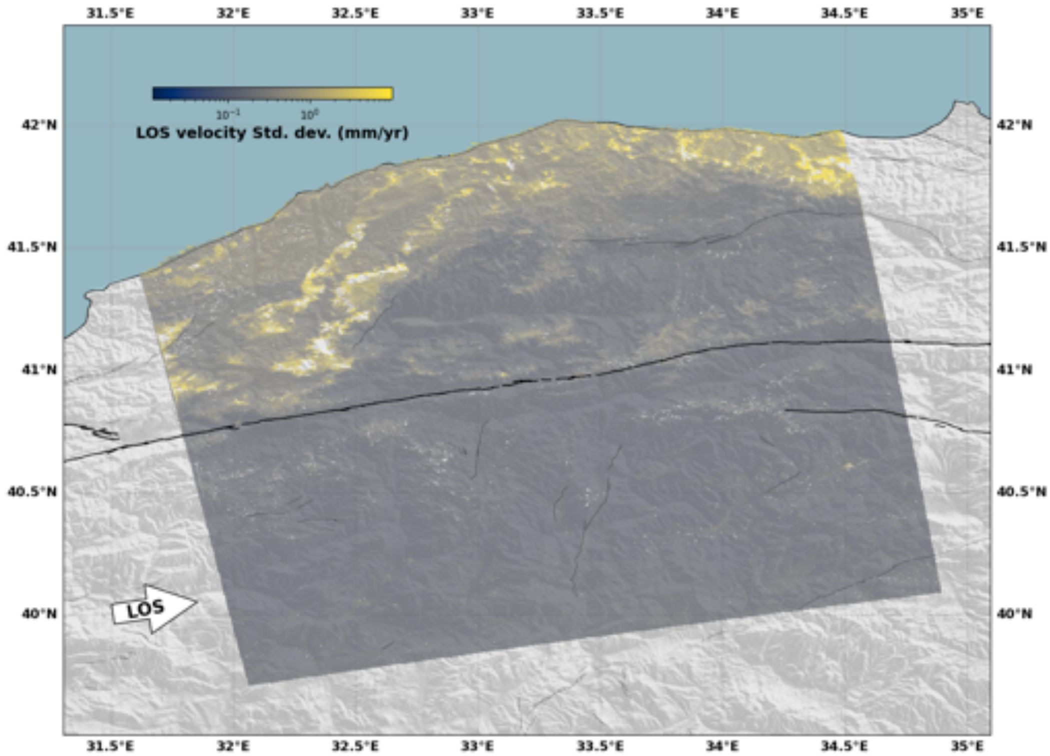

Figure S-8: **Line-of-sight velocity standard deviation map from track 87 -** Standard deviations are from the analyzed state covariance at the end of the Kalman filtering procedure.

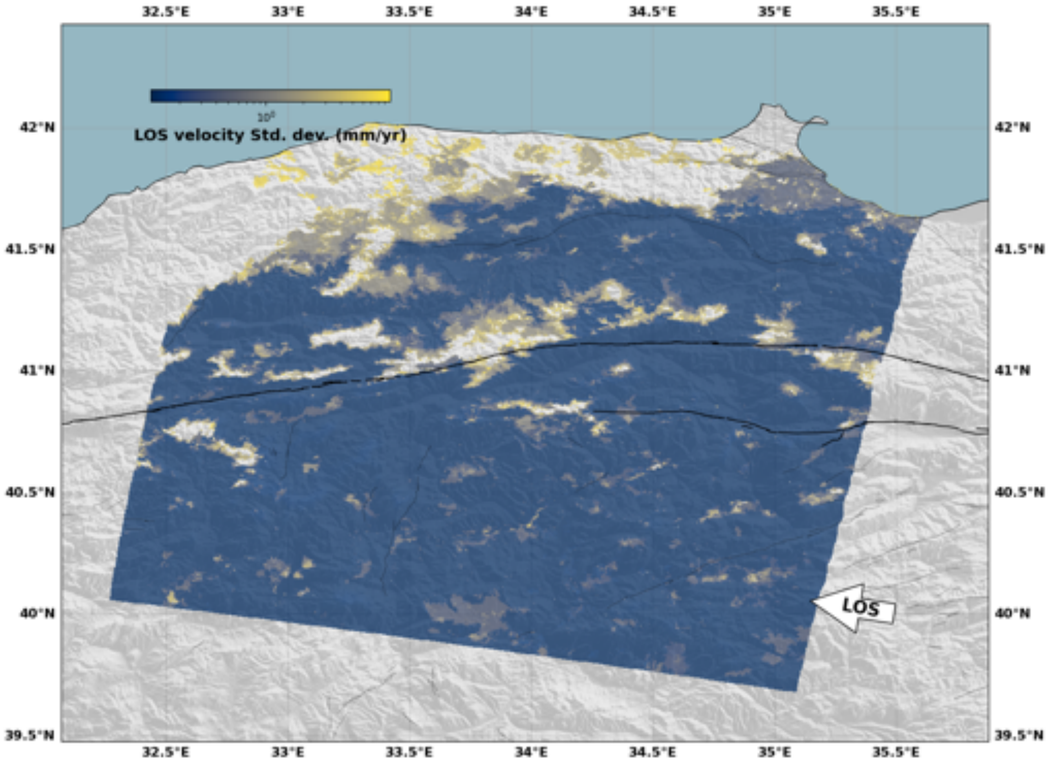

Figure S-9: **Line-of-sight velocity map standard deviation from track 167 -** Standard deviations are from the analyzed state covariance at the end of the Kalman filtering procedure.

1.4 Number of data per pixel

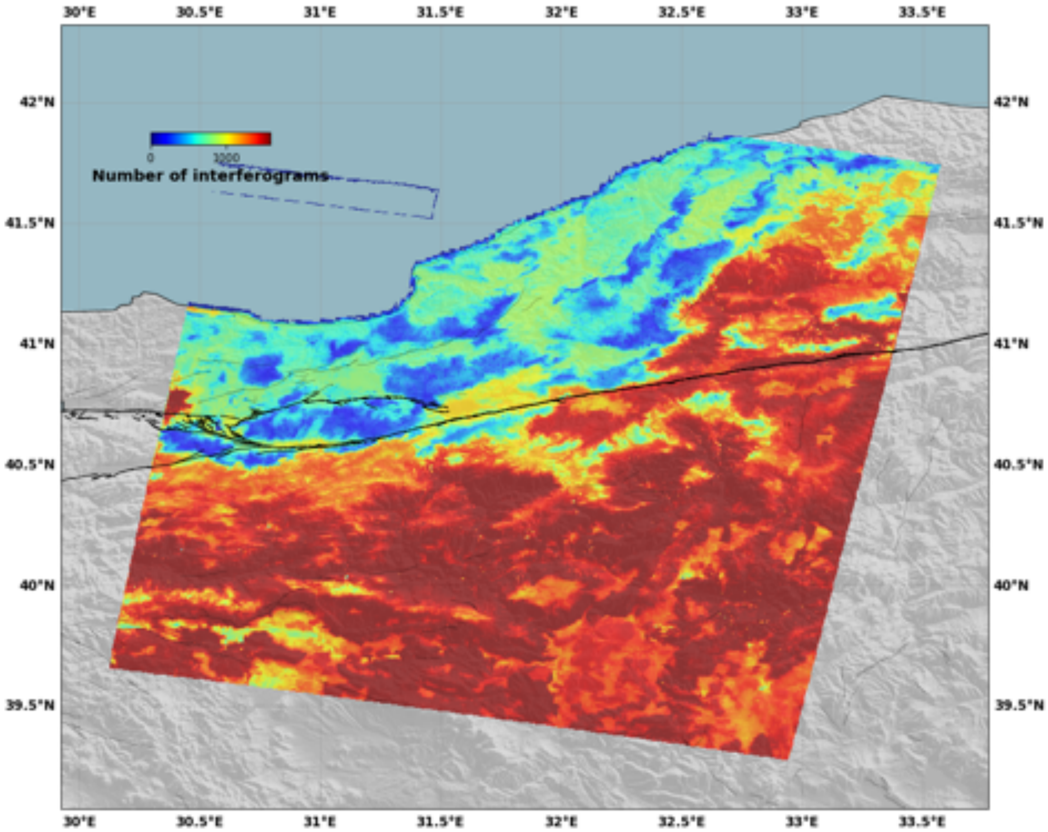

Figure S-10: **Number of interferograms available per pixels on track 65 -** Map of the number of unwrapped interferograms per pixel, used as one of the quality factor for pixel selection.

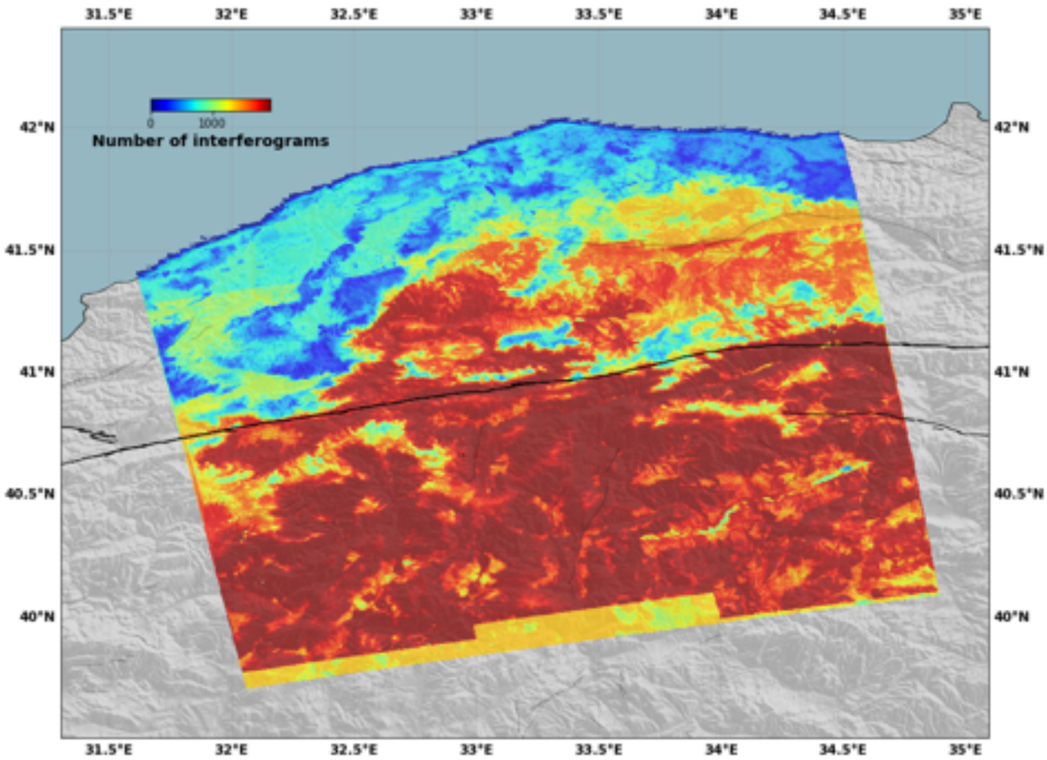

Figure S-11: **Number of interferograms available per pixels on track 87 -** Map of the number of unwrapped interferograms per pixel, used as one of the quality factor for pixel selection.

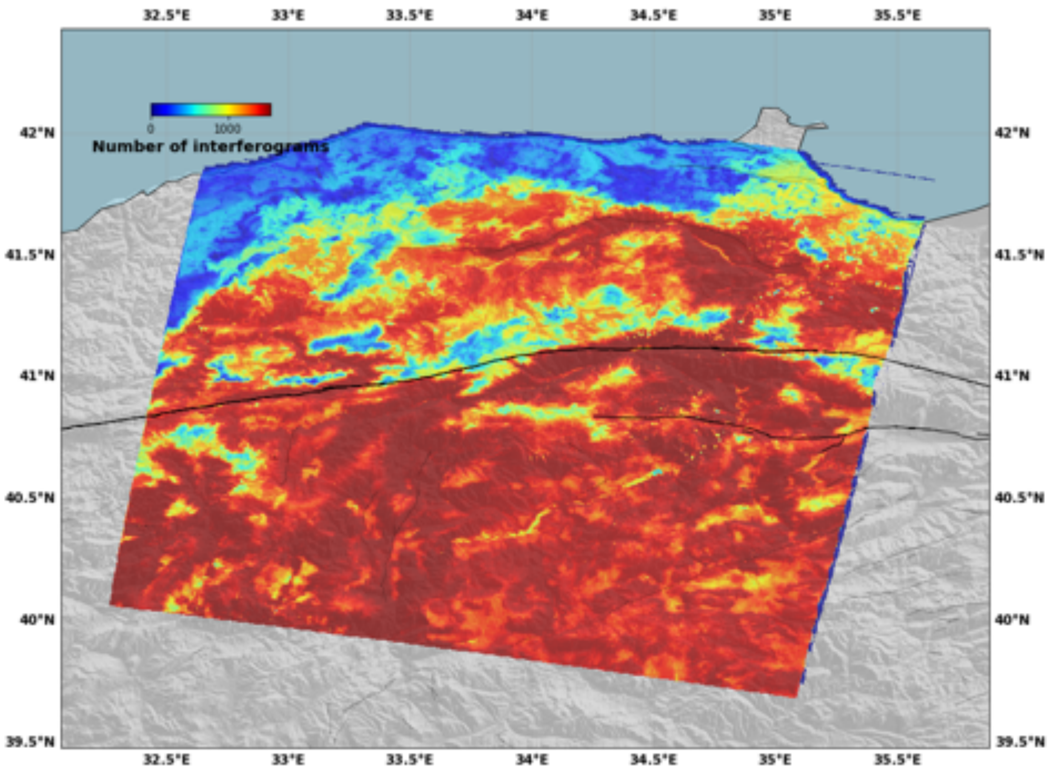

Figure S-12: **Number of interferograms available per pixels on 167 -** Map of the number of unwrapped interferograms per pixel, used as one of the quality factor for pixel selection.

1.5 RMS of time series reconstruction per pixel

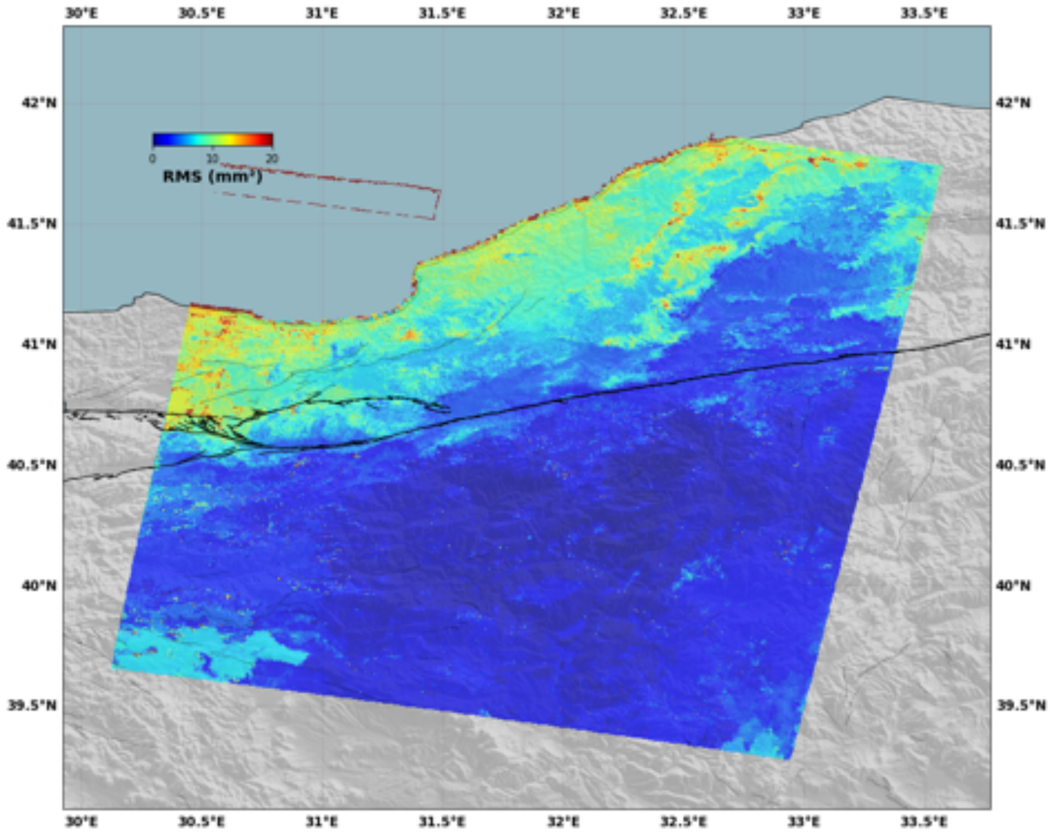

Figure S-13: **RMS of time series reconstruction for track 65 -** RMS is defined as the average of the square difference between data (i.e. interferograms) and time series reconstructions (i.e. interferograms predicted from the time series) and used as a quality factor for pixel selection.

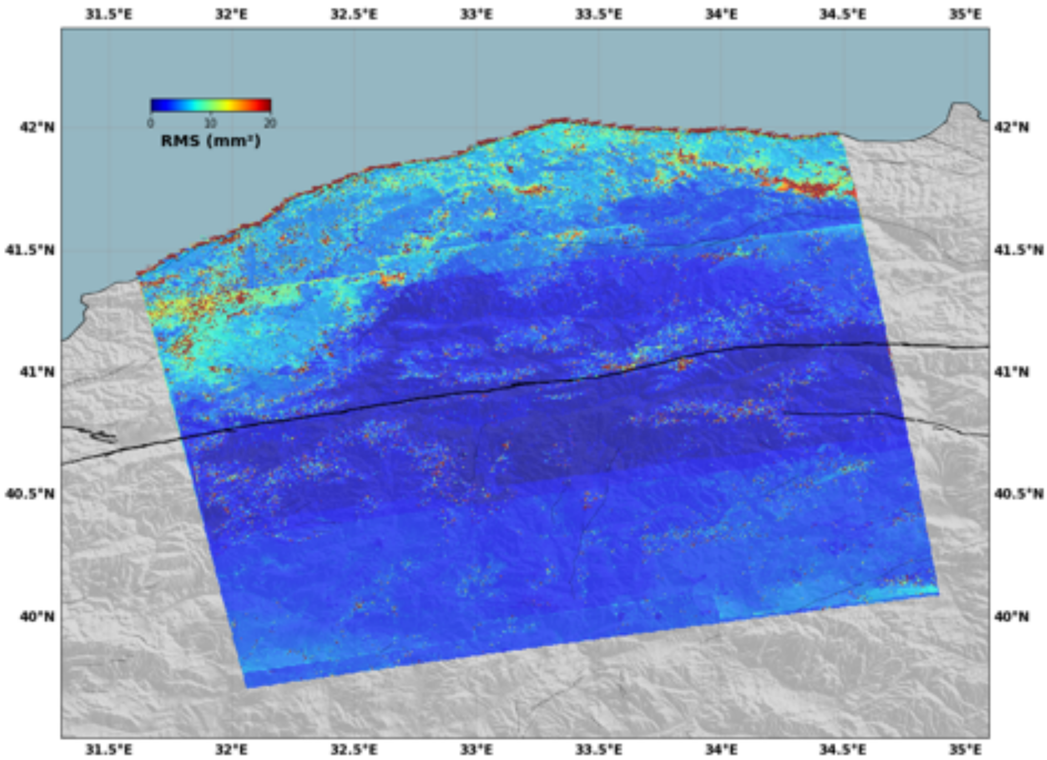

Figure S-14: **RMS of time series reconstruction for track 87 -** RMS is defined as the average of the square difference between data (i.e. interferograms) and time series reconstructions (i.e. interferograms predicted from the time series) and used as a quality factor for pixel selection.

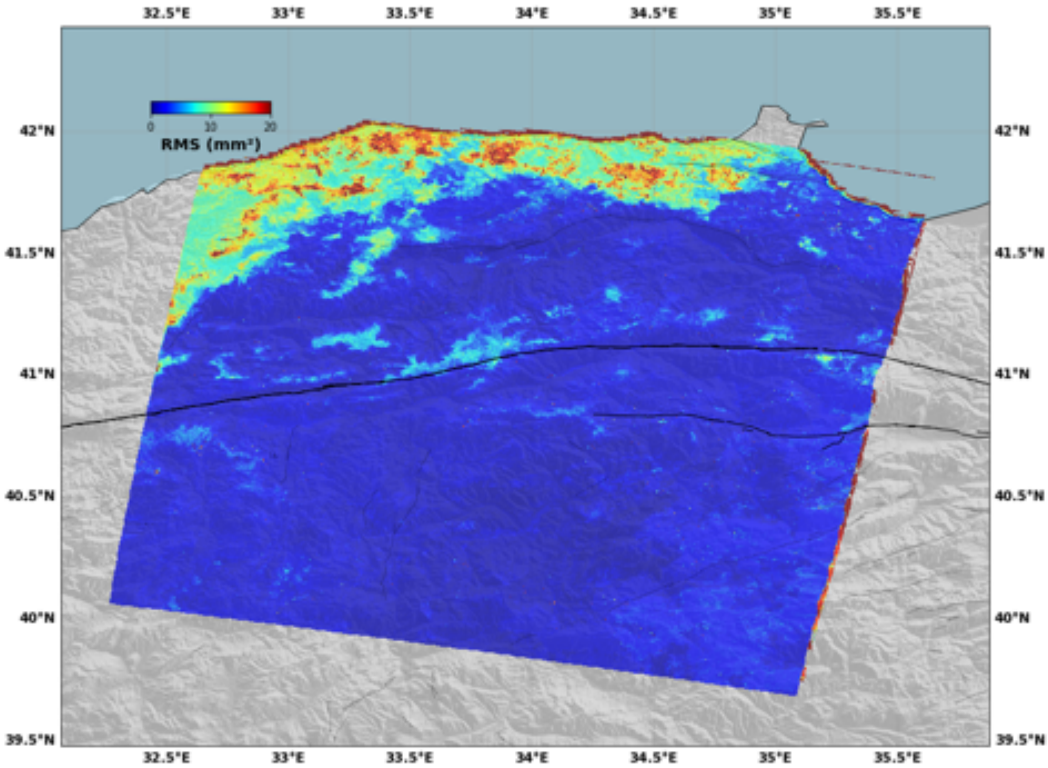

Figure S-15: **RMS of time series reconstruction for 167 -** RMS is defined as the average of the square difference between data (i.e. interferograms) and time series reconstructions (i.e. interferograms predicted from the time series) and used as a quality factor for pixel selection.

1.6 Additional results

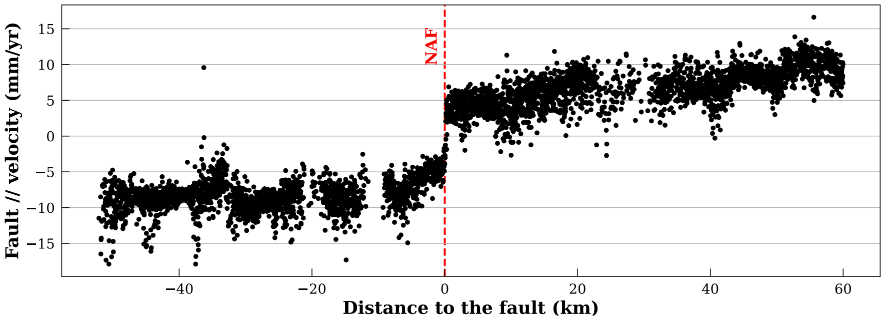

Figure S-16: **Fault perpendicular profile of fault parallel ground velocity -** This profile intersects the North Anatolian Fault in Ismetpasa.

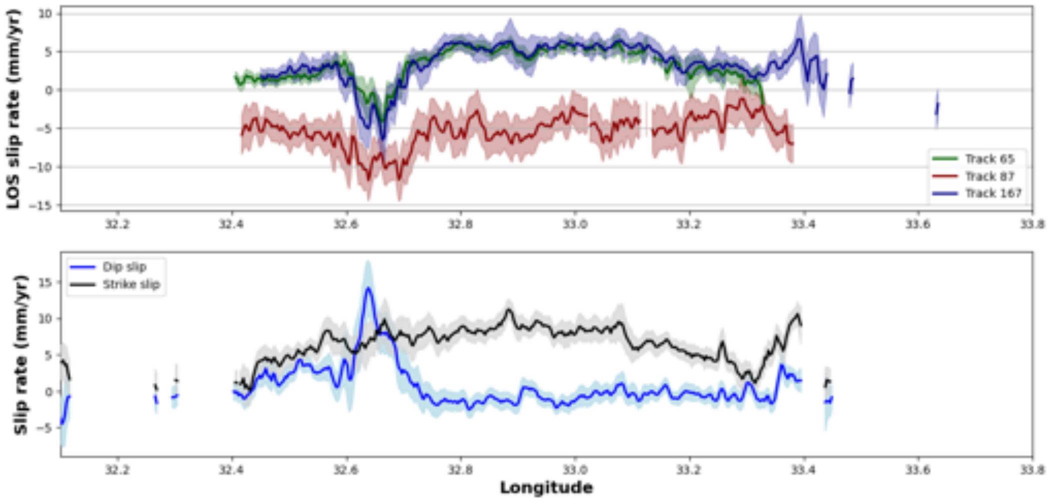

Figure S-17: **Along strike distribution of slip - Top** Along strike distribution of phase difference across the NAF in LOS for tracks 65 (green), 87 (red) and 167 (blue). Tracks 65 and 167 are both in the same geometry of acquisition (i.e. descending orbit), hence the remarkable agreement between the two independent datasets. Track 87 is along an ascending orbit. When motion is opposite on ascending and descending tracks LOS, ground motion is mostly horizontal as expected motion is aligned with the LOSs. When motion is opposite in LOS, ground motion is mostly vertical. **Bottom** Along strike distribution of horizontal and differential motion from the decomposition of the three tracks. As shown by the agreement between data shown above, ground motion is mostly horizontal (right lateral strike slip) along the fault with some vertical differential motion near Ismetpasa (northern block subsiding wrt. southern block).

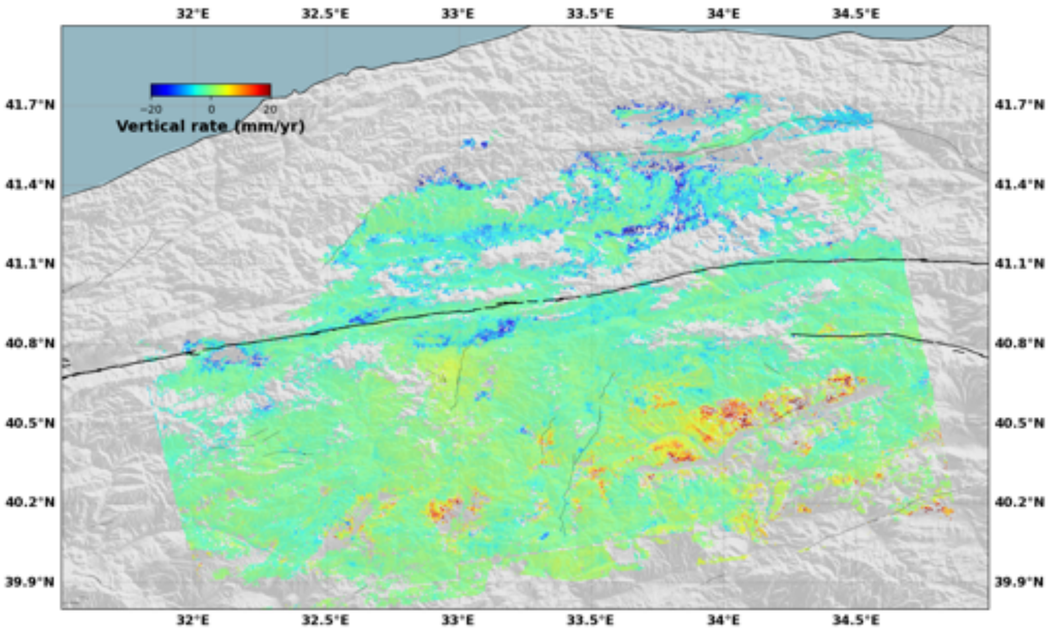

Figure S-18: **Map of vertical displacement rate -** This map results from the combination of the three velocity maps on track 65, 87 and 167.

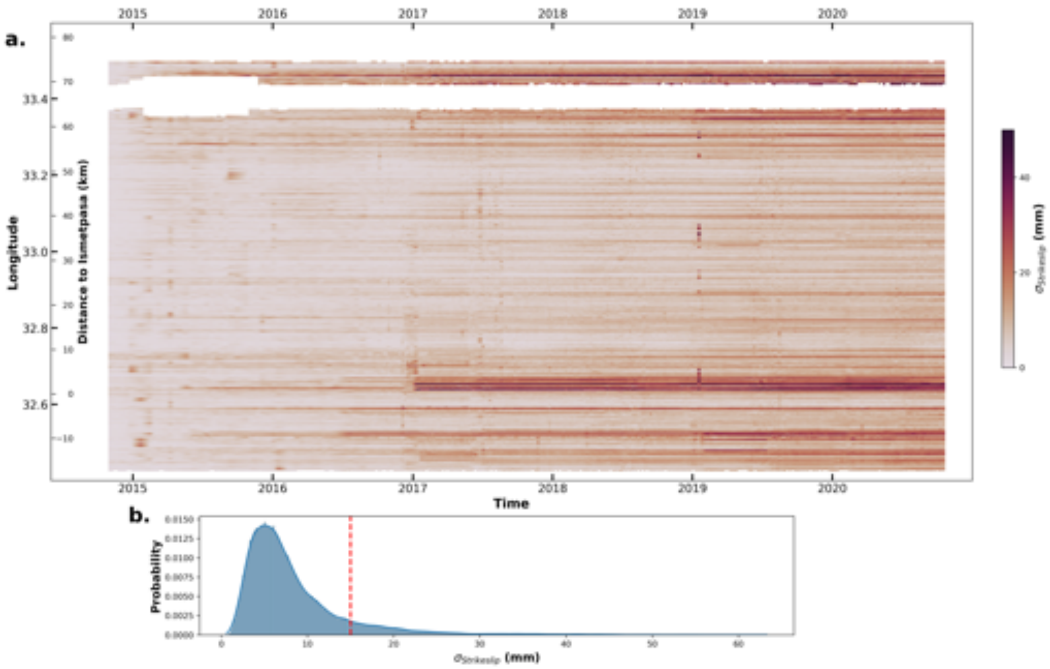

Figure S-19: **Uncertainties on strike slip motion -** Standard deviation of the strike slip motion as function of time. The uncertainty derives from the general least square inversion of the horizontal vs vertical relative motion between both sides of the fault. We consider the posterior covariance matrix and represent here the square root of the diagonal term. Bottom plot shows the distribution of these uncertainties with the threshold we have chosen for the representation in figure 4 of the main text.

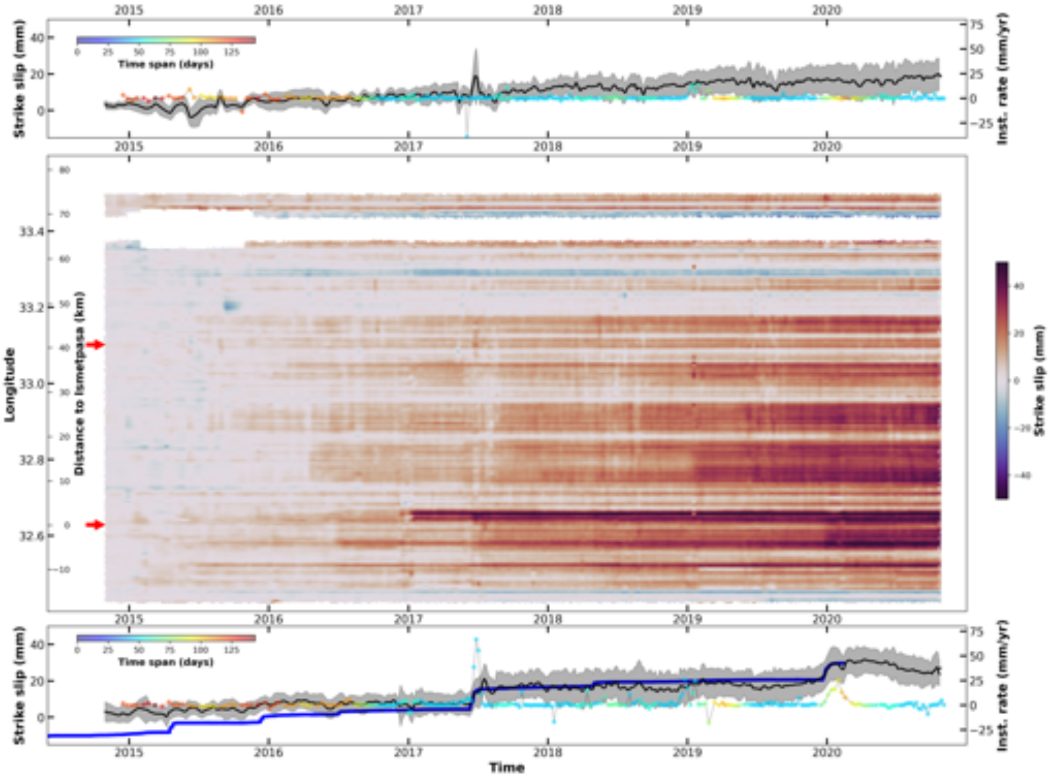

Figure S-20: **Time dependent surface slip rate -** Same as figure 4 of the main text without masking uncertain values.

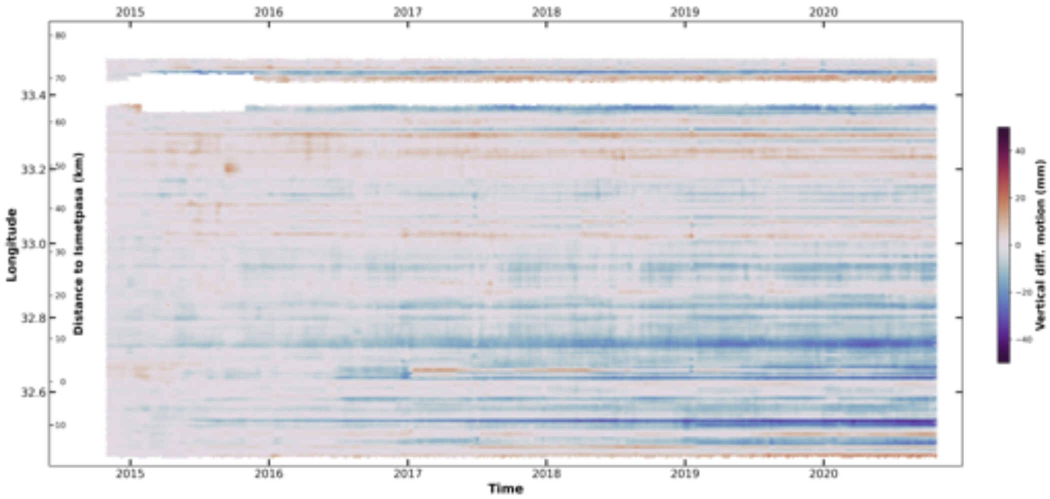

Figure S-21: **Time-dependent vertical differential motion -** Evolution of the vertical differential motion across the NAF. Blue indicates subsidence of the northern block wrt. the south.

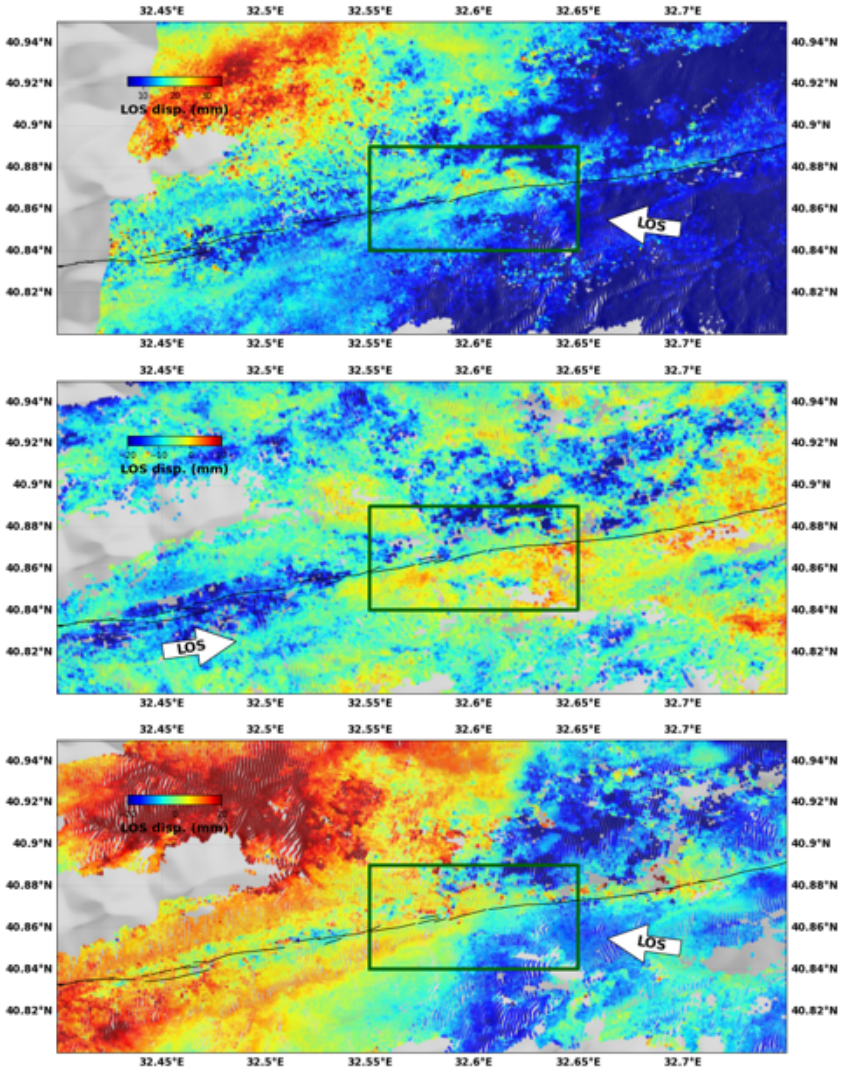

Figure S-22: **LOS displacement resulting from the slow slip event of 2017 -** Difference between time frames of the time series bracketing the slow slip event of 2017 from data on tracks 167 (top), 87 (center) and 65 (bottom). The white arrow indicates the direction from the satellite to the ground. Dark lines are fault traces. Dark rectangle indicates the region where the slow slip event is identified. The opposite sign of the across fault gradient between data on ascending and descending tracks confirms that motion is mainly horizontal.

2 GNSS dataset

We processed data from 77 continuous GNSS located in Eurasian (48 stations), Anatolian (21 stations), African (5 stations), Arabian (2 plates) and Somalia (1 station) Plates (Figure 1, a and b). We provide in table S-1 and S-2 the observation periods used in this paper and the measured velocities in the ITRF Eurasia-fixed reference frame, with our model predictions. Sites are grouped within the following networks:

- 8 GNSS from the International GNSS service, core network (`www.igs.org`): BHR4, CHUM, KIT3, MAT1, MDVJ, ONS1, POL2, RAMO, TASH
- 29 GNSS from the International GNSS service (`www.igs.org`): ADIS, ANKR, ARUC, BSHM, BUCU, CRAO, DJIG, DRAG, DYNG, GANP, GLSV, GRAZ, ISBA, ISTA, IZMI, KITG, KRS1, MERS, MIKL, NICO, ORID, PENC, POLV, SOFI, SULP, TEHN, TUBI, WARN, ZECK.
- 20 GNSS from the Turkish National Network (`https://www.tusaga-aktif.gov.tr/`): BOLU, BOL1, BOYT, CANK, CMLD, CORU, ESKS, HEND, HYMN, INE2, KKAL, KRBK, KSTM, KURU, NAHA, SIH1, SINP, SUNL, VEZI, ZONG.
- 19 GNSS from the ISMENET network: IS01, IS02, IS03, IS04, IS05, IS07, IS08, IS09, IS10, IS11, IS12, IS13, IS14, IS16, IS17, IS18, IS19, IS20, IS21. Each station of Ismenet includes a Zephyr geodetic antenna bolted in a boulder or custom made concrete monument and a NetR9 or NetRS receiver (Trimble) recording at 30 seconds, powered by either local power or solar panels. Antennas are covered by a radome.

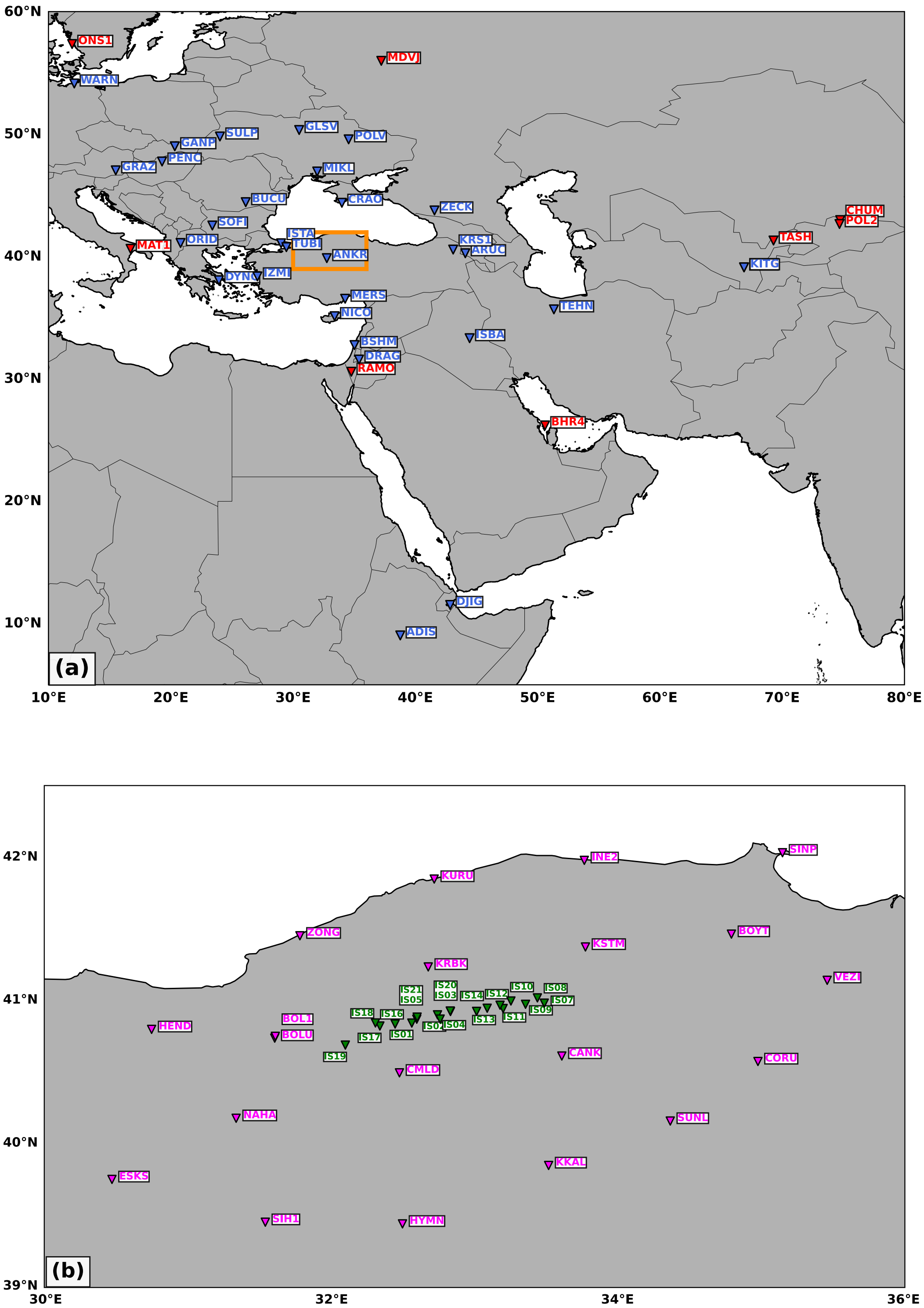

Figure S-23: **Selection of GNSS sites - a.** Extended selection including IGS, core network, sites (red) and IGS stations (blue). **b.** Local selection with sites from the Turkish Nation Network (pink) and from our ISMENET network (green).

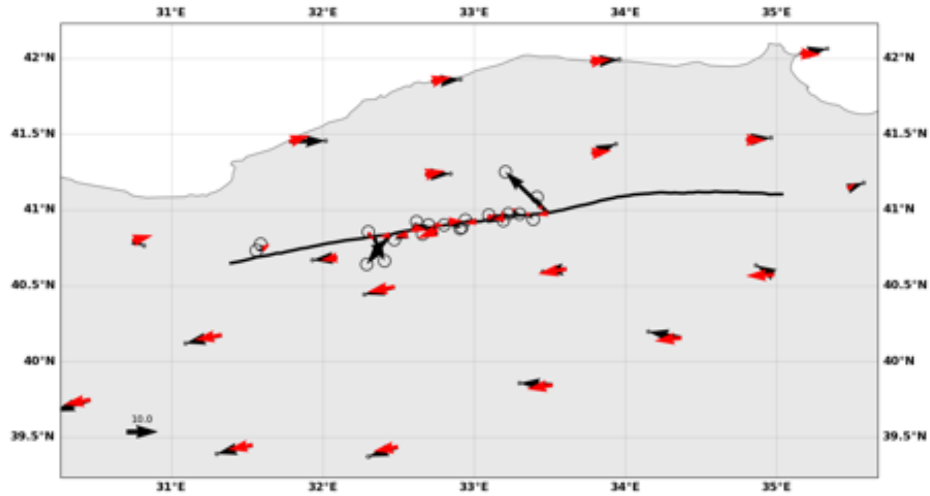

Figure S-24: **GNSS derived velocities and predictions from the mean model -** Map of the GNSS-derived velocities (black) together with the predictions from the mean model. Ellipses are 1-sigma. It is important to note that the mean model is not a model drawn from the posterior PDF, hence its predictions are not necessarily the best ones. In addition, error ellipses here only represent the formal uncertainties on the GNSS measurements feeding in $\mathbf{C}_d$ while our Bayesian approach assumes larger uncertainties deriving from the prediction error, $\mathbf{C}_p$.

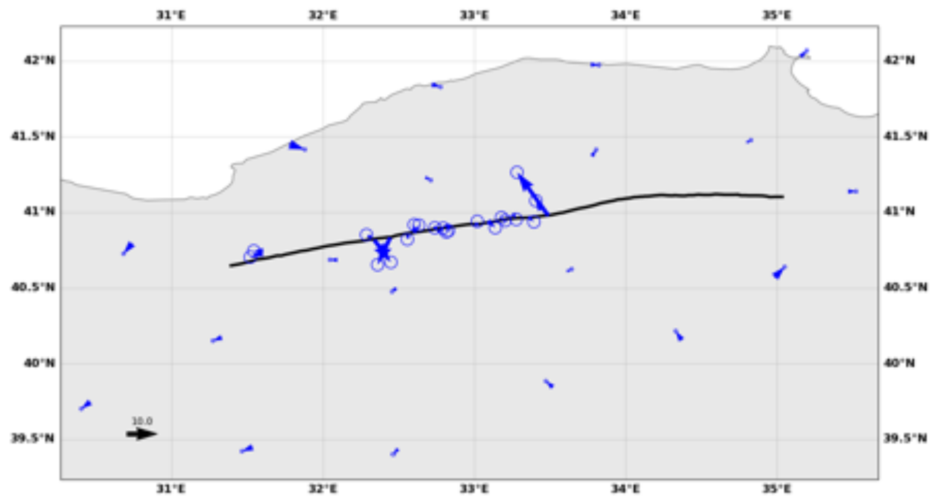

Figure S-25: **Residuals from the mean model -** Map of the residuals, as differences between velocities (black arrows on figure S-24) and predictions from the mean model (red arrows on figure S-24). Ellipses are 1-sigma. It is important to note that the mean model is not a model drawn from the posterior PDF, hence its predictions are not necessarily the best ones. In addition, error ellipses here only represent the formal uncertainties on the GNSS measurements feeding in $\mathbf{C}_d$ while our Bayesian approach assumes larger uncertainties deriving from the prediction error, $\mathbf{C}_p$.

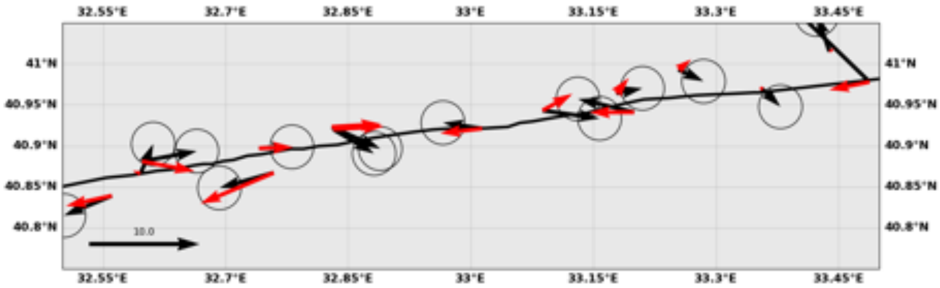

Figure S-26: **GNSS derived velocities and predictions from the mean model (close up) -** Map of the GNSS-derived velocities (black) together with the predictions from the mean model. Ellipses are 1-sigma. It is important to note that the mean model is not a model drawn from the posterior PDF, hence its predictions are not necessarily the best ones. In addition, error ellipses here only represent the formal uncertainties on the GNSS measurements feeding in $\mathbf{C}_d$ while our Bayesian approach assumes larger uncertainties deriving from the prediction error, $\mathbf{C}_p$.

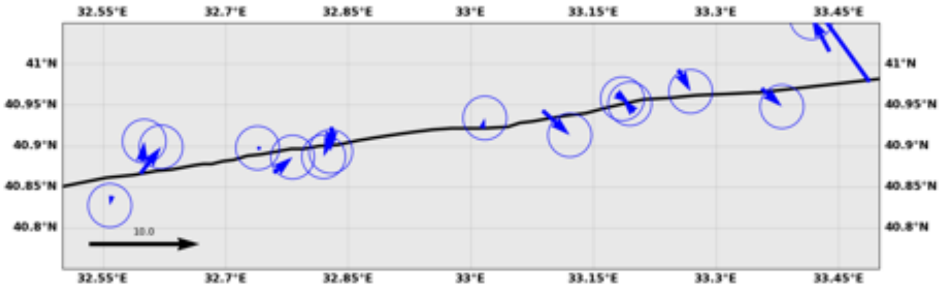

Figure S-27: **Residuals from the mean model (close up)-** Map of the residuals, as differences between velocities (black arrows on figure S-24) and predictions from the mean model (red arrows on figure S-24). Ellipses are 1-sigma. It is important to note that the mean model is not a model drawn from the posterior PDF, hence its predictions are not necessarily the best ones. In addition, error ellipses here only represent the formal uncertainties on the GNSS measurements feeding in $\mathbf{C}_d$ while our Bayesian approach assumes larger uncertainties deriving from the prediction error, $\mathbf{C}_p$.

NAME	Lon (^{o})	Lat (^{o})	First Obs (dec year)	Last Obs (dec year)
BOL1	31.606	40.746	2018.884	2021.578
BOLU	31.602	40.734	2016.534	2018.774
BOYT	34.797	41.461	2016.534	2021.578
CANK	33.610	40.609	2016.534	2021.578
CMLD	32.475	40.491	2016.534	2021.578
CORU	34.982	40.570	2016.534	2021.578
ESKS	30.464	39.746	2016.534	2021.578
HEND	30.741	40.795	2016.534	2021.578
HYMN	32.496	39.435	2016.534	2020.750
INE2	33.768	41.977	2016.534	2020.127
KKAL	33.518	39.843	2016.534	2021.578
KRBK	32.676	41.232	2016.534	2021.578
KSTM	33.776	41.371	2016.534	2021.578
KURU	32.718	41.846	2016.534	2021.578
NAHA	31.332	40.173	2016.534	2021.578
SIH1	31.536	39.447	2016.534	2021.578
SINP	35.154	42.030	2016.534	2021.578
SUNL	34.369	40.154	2016.534	2020.059
VEZI	35.467	41.138	2016.534	2021.578
ZONG	31.778	41.450	2016.534	2021.578
IS01	32.561	40.839	2016.537	2021.578
IS02	32.741	40.897	2016.534	2021.578
IS03	32.832	40.920	2016.534	2019.453
IS04	32.759	40.867	2016.542	2021.578
IS05	32.596	40.866	2016.944	2019.448
IS07	33.488	40.978	2019.456	2021.578
IS08	33.439	41.015	2019.456	2021.578
IS09	33.356	40.970	2019.456	2021.578
IS10	33.254	40.993	2019.456	2021.578
IS11	33.200	40.941	2019.440	2021.578
IS12	33.178	40.964	2019.440	2021.578

IS13	33.088	40.943	2019.462	2021.578
IS14	33.014	40.921	2019.442	2021.578
IS16	32.444	40.833	2019.451	2021.578
IS17	32.338	40.818	2019.451	2021.578
IS18	32.307	40.840	2019.445	2021.578
IS19	32.096	40.685	2019.445	2021.578
IS20	32.830	40.923	2019.456	2021.578
IS21	32.598	40.881	2019.451	2021.578

Table S-1: **GNSS observation period -** Period of observation for the stations used in this study. Sites with names starting with IS have been installed over the duration of the Geo4D project.

Site	**Lon**	**Lat**	**Data** (mm/yr)		**Ref. removed** (mm/yr)		**Model** (mm/yr)	
	(°E)	(°N)	East	North	East	North	East	North
BOL1	31.606	40.746	-11.288	1.658	-0.812	1.364	2.333	1.425
BOLU	31.602	40.734	-12.533	0.150	-2.058	-0.144	2.032	1.375
BOYT	34.797	41.461	-2.306	1.212	8.235	0.699	6.768	-0.107
CANK	33.610	40.609	-18.258	-0.437	-7.795	-0.869	-9.410	-1.626
CMLD	32.475	40.491	-20.448	-2.175	-9.996	-2.529	-9.063	-1.735
CORU	34.982	40.570	-16.440	3.662	-5.979	3.135	-9.325	-0.321
ESKS	30.464	39.746	-22.154	-3.658	-11.767	-3.871	-8.779	-1.599
HEND	30.741	40.795	-6.565	-1.383	3.917	-1.617	6.812	1.830
HYMN	32.496	39.435	-20.045	-2.878	-9.689	-3.233	-8.104	-1.467
INE2	33.768	41.977	-0.994	1.224	9.593	0.782	6.868	0.897
KKAL	33.518	39.843	-21.268	1.046	-10.875	0.620	-8.596	-1.381
KRBK	32.676	41.232	-2.085	0.631	8.434	0.263	6.625	1.256
KSTM	33.776	41.371	-2.482	3.587	8.050	3.144	6.638	0.991
KURU	32.718	41.846	-0.953	1.058	9.622	0.687	6.695	1.539
NAHA	31.332	40.173	-22.371	-2.478	-11.947	-2.752	-9.020	-1.634

SIH1	31.536	39.447	-22.170	-2.629	-11.812	-2.916	-8.289	-1.555
SINP	35.154	42.030	-1.619	2.183	8.974	1.647	6.933	-0.319
SUNL	34.369	40.154	-21.295	2.540	-10.873	2.055	-8.906	-0.973
VEZI	35.467	41.138	-5.164	2.521	5.349	1.962	2.693	1.947
ZONG	31.778	41.450	1.545	0.546	12.085	0.239	6.955	1.976
IS01	32.561	40.839	-14.892	-1.461	-4.408	-1.821	-4.220	-0.934
IS02	32.741	40.897	-7.470	0.490	3.019	0.118	3.148	0.093
IS03	32.832	40.920	-6.757	-1.834	3.734	-2.213	4.631	0.287
IS04	32.759	40.867	-15.465	-1.008	-4.979	-1.382	-6.709	-2.817
IS05	32.596	40.866	-9.314	3.076	1.172	2.714	-0.715	0.274
IS07	33.488	40.978	-24.545	14.010	-14.049	13.586	-3.717	-0.733
IS08	33.439	41.015	-11.663	3.820	-1.163	3.400	0.474	0.301
IS09	33.356	40.970	-8.766	-1.259	1.729	-1.674	-0.133	-0.016
IS10	33.254	40.993	-8.176	-0.664	2.322	-1.072	1.187	0.932
IS11	33.200	40.941	-15.648	1.616	-5.155	1.212	-4.080	-0.014
IS12	33.178	40.964	-8.079	0.865	2.416	0.463	1.159	1.418
IS13	33.088	40.943	-5.261	-0.326	5.232	-0.722	2.739	1.534
IS14	33.014	40.921	-14.088	0.928	-3.597	0.537	-3.850	-0.429
IS16	32.444	40.833	-18.174	-9.313	-7.691	-9.665	-3.527	-0.675
IS17	32.338	40.818	-6.993	-7.463	3.489	-7.807	-2.052	-0.390
IS18	32.307	40.840	-10.802	1.037	-0.318	0.695	0.673	0.148
IS19	32.096	40.685	-18.671	-0.552	-8.201	-0.880	-5.683	-0.940
IS20	32.830	40.923	-6.038	-1.609	4.453	-1.987	4.545	0.266
IS21	32.598	40.881	-5.467	1.295	5.020	0.933	4.823	-0.910

Table S-2: **GNSS data, corrected data and model -** Table of GNSS rates used in this article. Data refers to the original GNSS velocities in the Eurasia-fixed referenced frame. Ref. removed refers to the original velocities corrected from the translation and rotation term inferred in the inversion procedure. Model refers to the displacement rates predicted by the slip model. Sites with names starting with IS have been installed over the duration of the Geo4D project.

3 Model additional information and performance

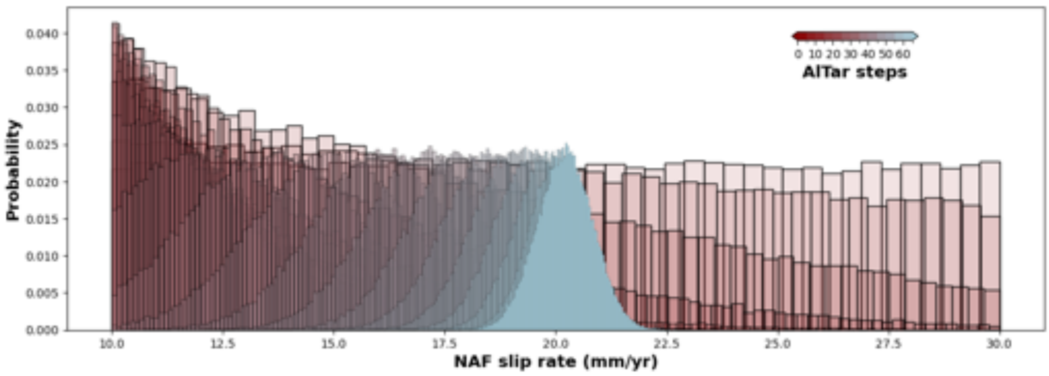

Figure S-28: **Example of convergence during tempering -** While the sampler marches forward, it progressively shrinks the sample set onto the final, posterior PDF. Here, we show the marginal PDF of the deep slip rate on the NAF, which transitions at each step from the a priori uniform distribution to the posterior, which, in this case, is a Gaussian distribution.

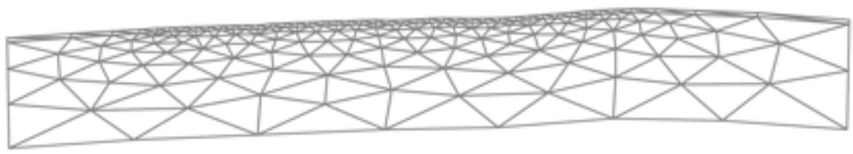

Figure S-29: **Triangular mesh for the shallow part of the NAF -** 3D representation of the triangular mesh used for the shallow section of the NAF. Shallowest triangles are 1 km-sized while largest, deepest ones are 10 km-size. Shallowest row intersects the surface while deepest row reaches 20 km.

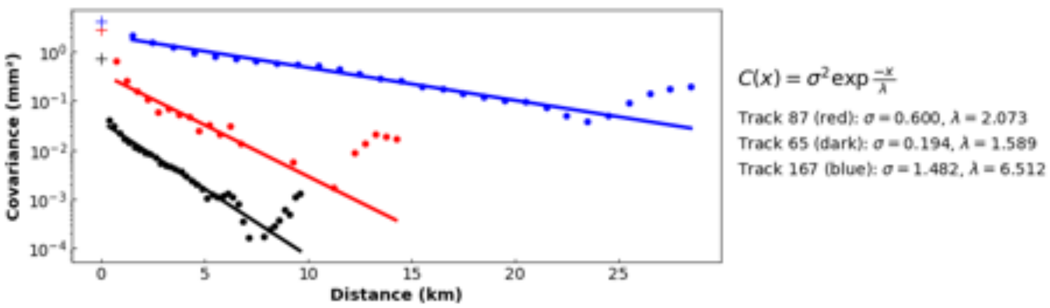

Figure S-30: **Covariance functions for the InSAR velocity maps -** Empirical covariances of the velocity maps from tracks 65 (dark), 87 (red) and 167 (red). Dots are the empirical covariances. Lines are the exponential fit to the covariance functions. Crosses are the variance of the data (auto-correlation).

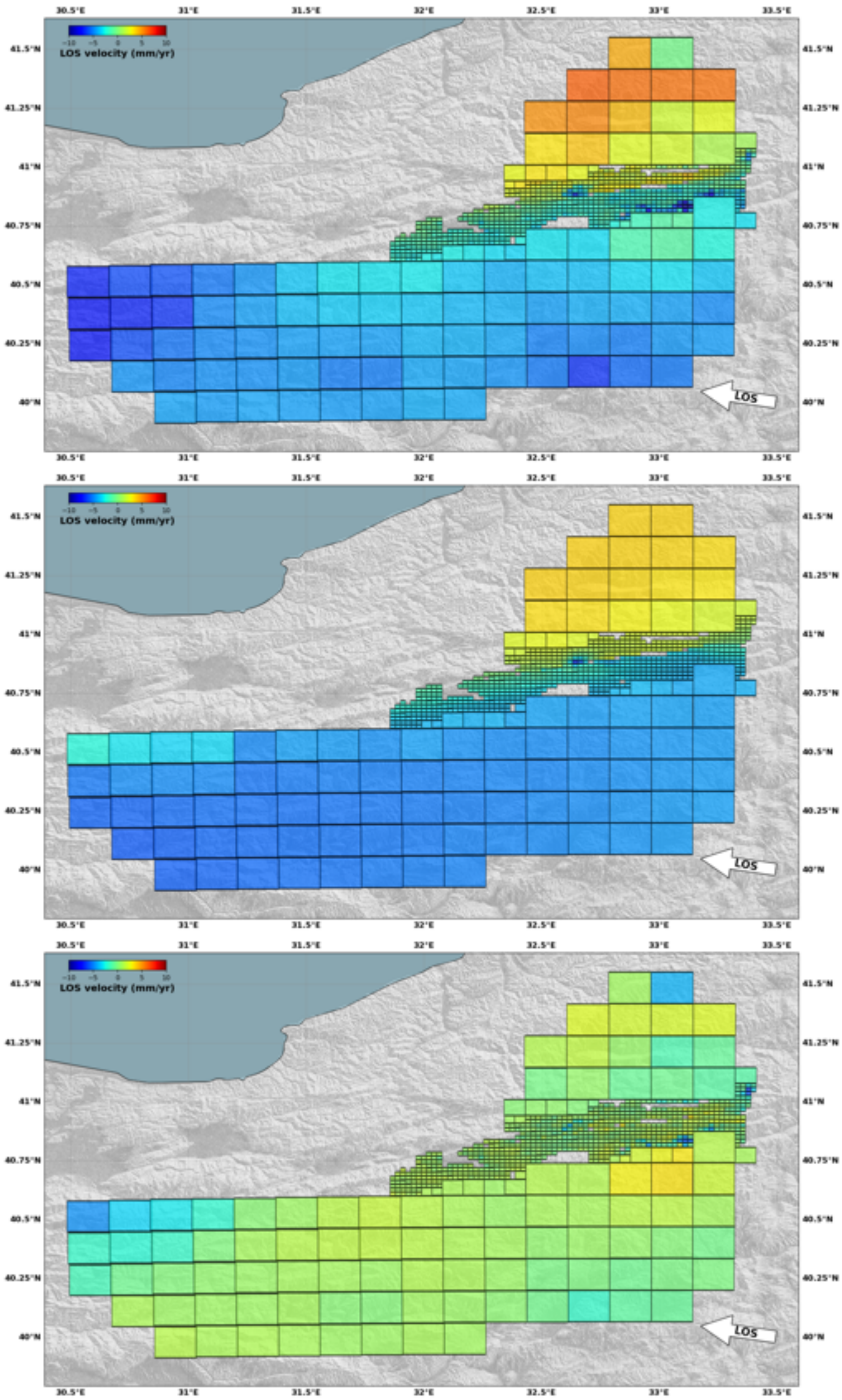

Figure S-31: **Decimated velocity field from track 65 -** Decimation geometry and resulting input data set for the slip rate inversion (top), prediction from the mean model (center) and residuals (bottom).

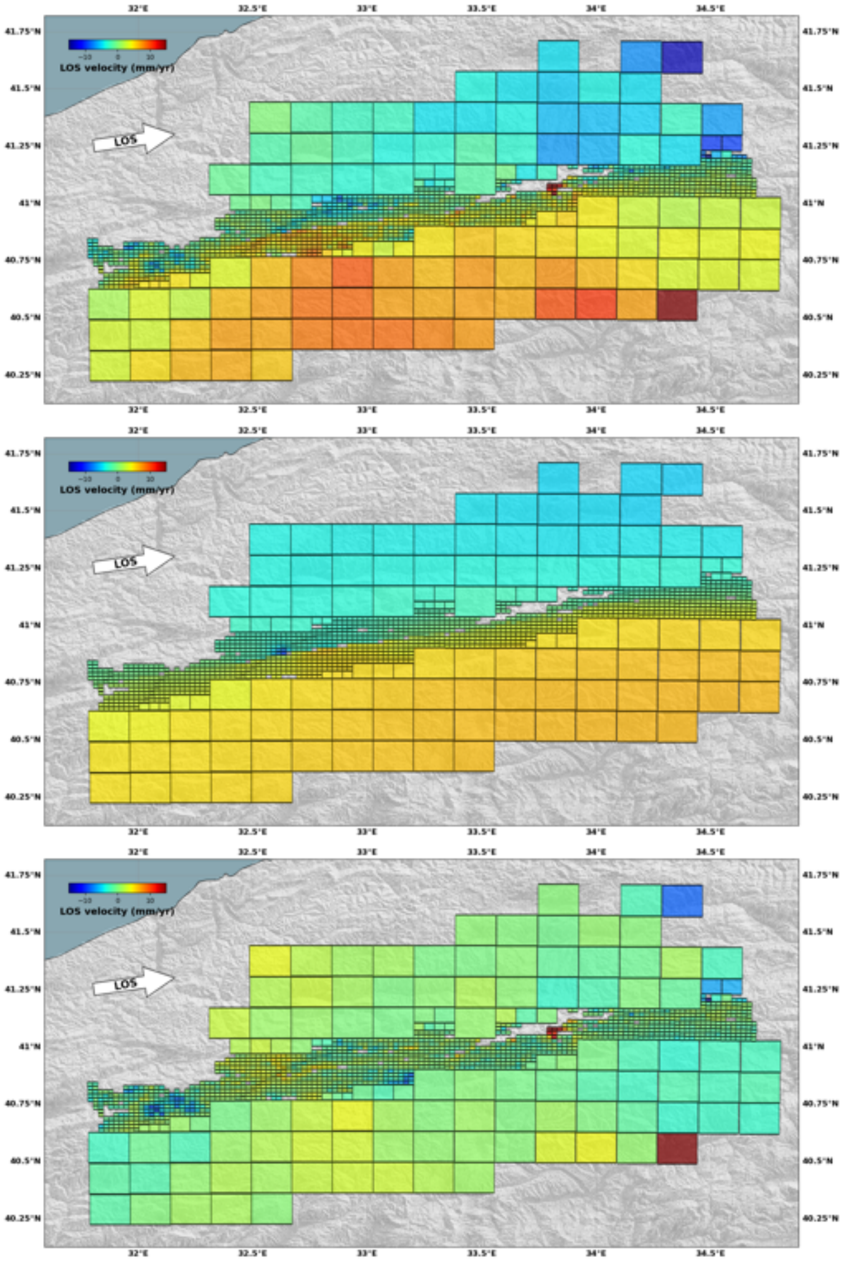

Figure S-32: **Decimated velocity field from track 87 -** Decimation geometry and resulting input data set for the slip rate inversion (top), prediction from the mean model (center) and residuals (bottom).

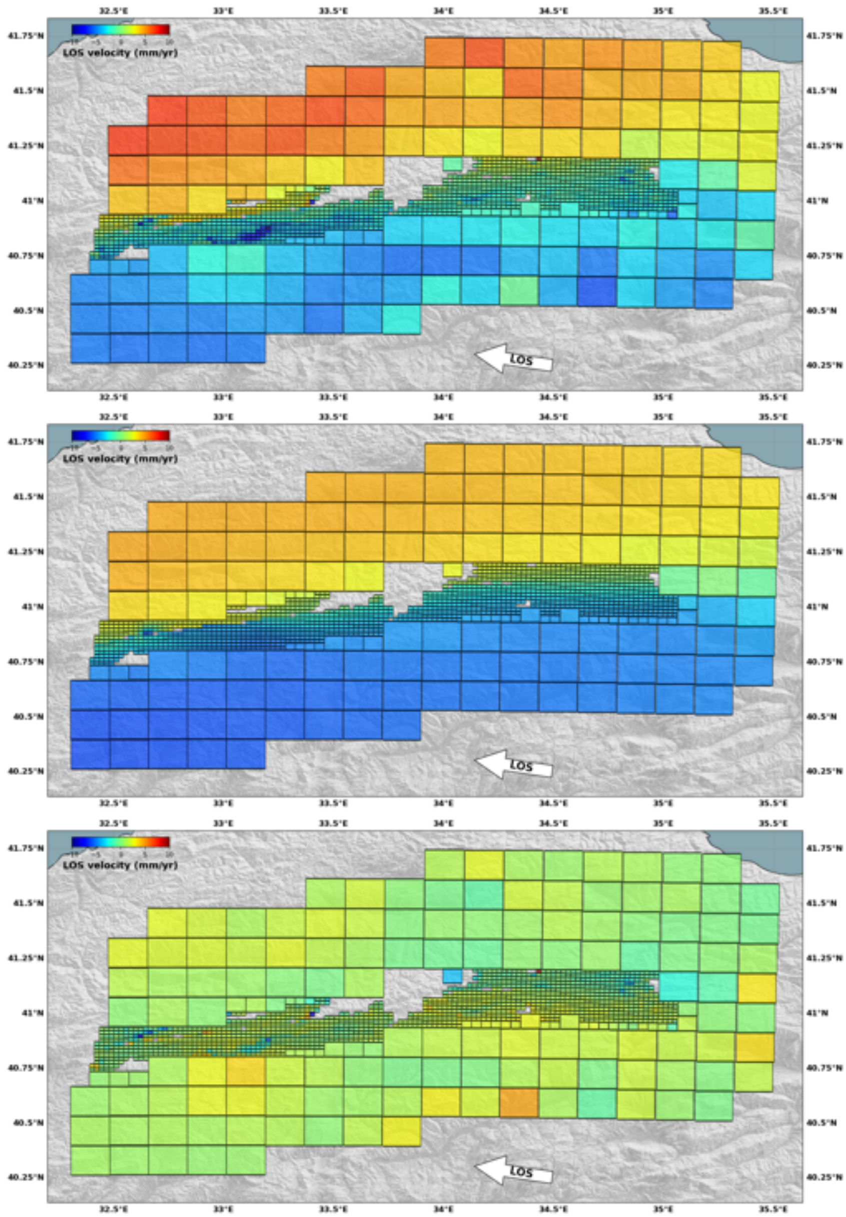

Figure S-33: **Decimated velocity field from track 167 -** Decimation geometry and resulting input data set for the slip rate inversion (top), prediction from the mean model (center) and residuals (bottom).

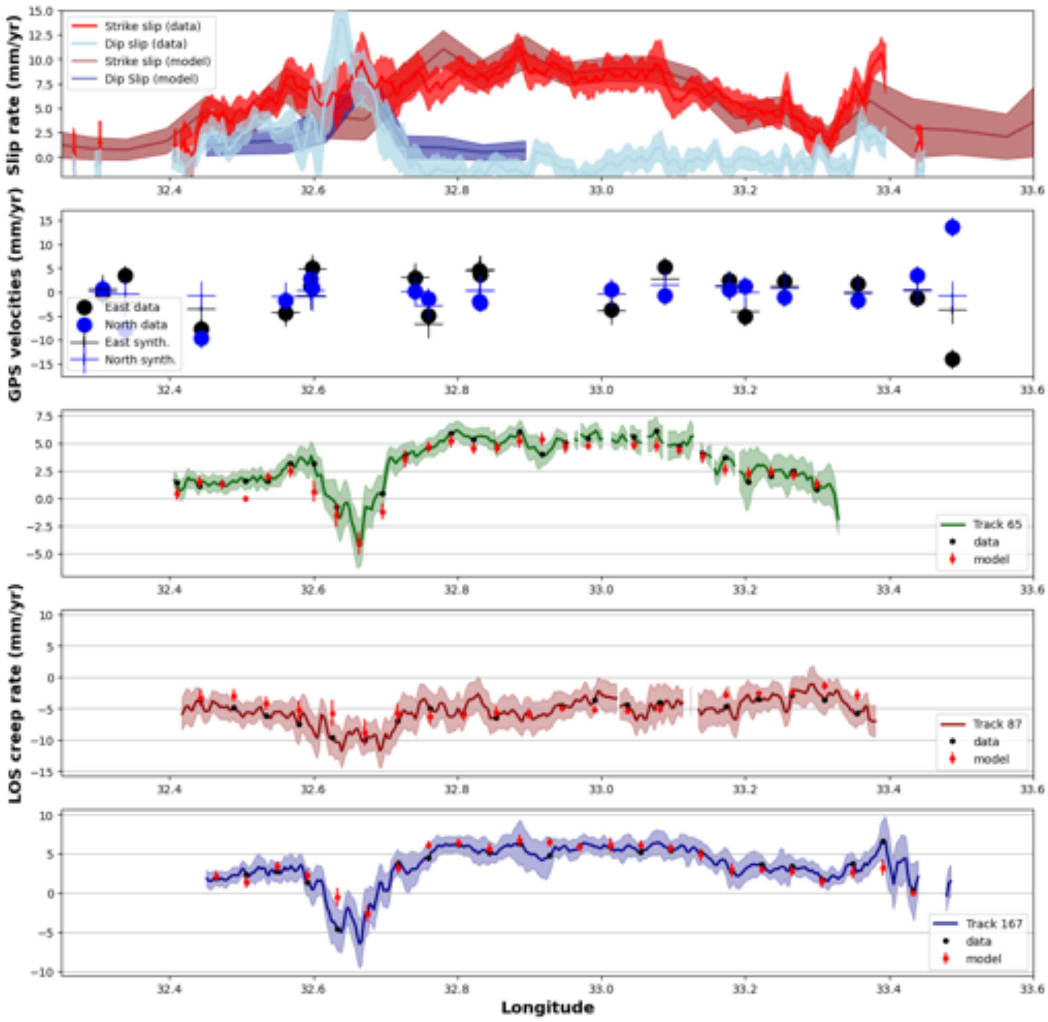

Figure S-34: **Fit to the surface fault slip data - Top** Surface slip rate measured on the horizontal and vertical ground motion maps and surface slip rate from the posterior PDF of the slip rate model. Red is for strike slip and blue for vertical differential motion (i.e. dip slip). **Second** Data (circles) and predictions from the mean model (crosses) for the GNSS data along the fault in the east (black) and north (blue) directions. **Three bottom plots** Data (lines) and predictions from the mean model for the surface slip measured on InSAR velocity maps.

4 Slip rates at Ismetpasa

All slip rates from table S-3 were measured within a short distance from the city of Ismetpasa. Most of these measurements were made within the city, at the train station, while some of them average over a distance difficult to estimate, depending on the publication. Refer to Bilham et al. (2016) for a detailed description of these surface slip rates. Rates are from Ambraseys (1970), Aytun (1982), Eren (1984), Deniz et al. (1993), Altay and Sav (1991), Çakir et al. (2005), Kutoglu and Akcin (2006), Kutoglu et al. (2008), Kutoglu et al. (2010), Karabacak et al. (2011), Deguchi (2011), Ozener et al. (2013) and Kaneko et al. (2012). Some rates were re-evaluated by Bilham et al. (2016). We have manually digitized figure 5 of Altay and Sav (1991).

Time	**Creep rate mm/yr**	**Std dev mm/yr**	**Observation Period start - end**	**Source**	**Measurement type**
1963	10.40	0.40	1957-1969	Ambraseys (1970)	Wall offset (photo)
1975	10.80	0.40	1969-1979	Aytun (1982)	Triangulation
1977	10.20	0.60	1972-1979	Eren (1984)	Trilateration
1987	9.30	0.70	1982-1992	Deniz et al. (1993)	Trilateration
1997	7.80	0.50	1992-2002	Kutoglu and Akcin (2006)	GNSS
1986	7.30	0.10	1982-1990	Altay and Sav (1991)	Creepmeter
2004	12.00	1.30	2002-2007	Kutoglu et al. (2008)	GNSS
2007	15.10	4.10	2007-2008	Kutoglu et al. (2010)	GNSS
1996	8.00	3.00	1992-2001	Çakir et al. (2005)	InSAR
2008	8.35	0.24	2003-2011	Cetin et al. (2014)	InSAR
2009	8.40	1.60	2007-2009	Karabacak et al. (2011)	LiDAR
2008	7.60	1.10	2005-2011	Ozener et al. (2013)	GNSS
2009	9.00	1.00	2007-2011	Kaneko et al. (2013)	InSAR
1992	8.30	0.10	1969-2016	Bilham et al. (2016)	Wall offset
1999	7.10	0.30	1984-2016	Bilham et al. (2016)	Wall offset
1976	9.90	0.30	1969-1984	Bilham et al. (2016)	Wall offset (photo)
2015	5.90	0.10	2014-2016	Bilham et al. (2016)	Creepmeter
2015	6.10	1.00	2014-2016	Bilham et al. (2016)	Wall offset
2017	6.00	2.00	2014-2021	This study	S1 InSAR

Table S-3: **Slip rates at Ismetpasa -** Table of slip rates measured at Ismetpasa since the 1950's. Please be aware that this table is almost entirely a copy of that from Bilham et al 2016 and this paper should be cited whenever this table is used.

References

Altay, C., & Sav, H. (1991). Continuous creep measurement along the North Anatolian Fault zone. *Bulletin of the geological congres of Turkey*, *6*, 77–84.

Ambraseys, N. N. (1970). Some characteristic features of the Anatolian fault zone. *Tectonophysics*, *9*, 143–165.

Aytun, A. (1982). Creep Measurements in the Ismetpaşa Region of the North Anatolian Fault Zone. *Multidisciplinary Approach to Earthquake Prediction Progress in Earthquake Prediction Research*, *2*, 279–292.

Bilham, R., Ozener, H., Mencin, D., Dogru, A., ERGINTAV, S., CAKIR, Z., ... Mattioli, G. (2016). Surface creep on the North Anatolian Fault at Ismetpasa, Turkey, 1944-2016. *Journal of Geophysical Research-Solid Earth*, *121*, 7409–7431. doi: 10.1002/2016JB013394

Çakir, Z., Akoglu, A., Belabbes, S., Ergintav, S., & Meghraoui, M. (2005). Creeping along the Ismetpasa section of the North Anatolian fault (Western Turkey): Rate and extent from InSAR. *Earth and Planetary Science Letters*, *238*(1-2), 225–234. doi: 10.1016/j.epsl.2005.06.044

Deguchi. (2011). Detection of fault creep around naf by insar time series analysis using palsar data. *Proc. of SPIE, SAR Image Analysis, Modeling, and Techniques XI*, *8179*. doi: 10.1117/12.898478

Deniz, R., Aksoy, A., Yalin, D., Seeger, H., Franke, P., Hirsch, O., & Bautsch, P. (1993). Determination of crustal movements in turkey by terrestrial geodetic methods. *Journal of Geodynamics*, *18*(1), 13–22. doi: https://doi.org/10.1016/0264-3707(93)90024-Z

Eren, K. (1984). Strain analysis along the north analtolian fault by using geodetic surveys. *Bulletin géodésique*, *58*(2), 137–150. doi: 10.1007/BF02520898

Kaneko, Y., Fialko, Y., Sandwell, D. T., Tong, X., & Furuya, M. (2012). Interseismic deformation and creep along the central section of the North Anatolian fault (Turkey): InSAR observations and implications for rate-and-state friction properties. *Journal of Geophysical Research-Solid Earth*, *118*, 316– 331. doi: 10.1029/2012JB009661

Karabacak, V., Altunel, E., & Cakir, Z. (2011). Monitoring aseismic surface creep along the north anatolian fault (turkey) using ground-based lidar. *Earth and Planetary Science Letters*, *304*(1), 64–70. doi: 10.1016/j.epsl.2011.01.017

Kutoglu, H. S., & Akcin, H. (2006). Determination of the 30-year creep trend on the ismetpaşa segment of the north anatolian fault using an old geodetic network. *Earth, Planets and Space*, *58*(8), 937–942. doi: 10.1186/BF03352598

Kutoglu, H. S., Akcin, H., Gundogdu, O., Gormus, K. S., & Koksal, E. (2010, 12). Relaxation on the ismetpasa segment of the north anatolian fault after the golcuk $m_w = 7.4$ and duzce $m_w = 7.2$ shocks. *Nat. Hazards Earth Syst. Sci.*, *10*(12), 2653–2657. doi: 10.5194/nhess-10-2653-2010

Kutoglu, H. S., Akcin, H., Kemaldere, H., & Gormus, K. S. (2008, 12). Triggered creep rate on the ismetpasa segment of the north anatolian fault. *Nat. Hazards Earth Syst. Sci.*, *8*(6), 1369–1373. doi: 10.5194/nhess-8-1369-2008

Ozener, H., Dogru, A., & Turgut, B. (2013). Quantifying aseismic creep on the ismetpasa segment of the north anatolian fault zone (turkey) by 6 years of gps observations. *Journal of Geodynamics*, *67*, 72–77. doi: 10.1016/j.jog.2012.08.002